AFOSR-TR-~~96~~ 97

0126

REPORT DOCUMENTATION PAGE

1. AGENCY USE ONLY (Leave blank)

2. REPORT DATE
2/6/97

3. REPORT TYPE AND DATES COVERED
Final Technical 9/1/95 - 8/31/96

4. TITLE AND SUBTITLE OF REPORT
Instrumentation for Accurate Measurement and Control of Optical Phase for Time and Coherence Domain Communications and Space-Time Interferometry

5. FUNDING NUMBERS
3484/US
61103D

6. AUTHOR(S)
David J. Brady

7. PERFORMING ORGANIZATION NAME(S) AND ADDRESS(ES)
The Board of Trustees of the University of Illinois
c/o Grants & Contracts Office
801 S. Wright Street
Champaign, IL 61820

8. PERFORMING ORGANIZATION REPORT NUMBER:

9. SPONSORING/MONITORING AGENCY NAME(S) AND ADDRESS(ES)
AFOSR/NE
110 Duncan Avenue, Suite B115
Bolling AFB, DC 20332-0001

10. SPONSORING/MONITORING AGENCY REPORT NUMBER:
F49620-95-1-0496

11. SUPPLEMENTARY NOTES:

12a. DISTRIBUTION AVAILABILITY STATEMENT
APPROVED FOR PUBLIC RELEASE: DISTRIBUTION UNLIMITED

12b. DISTRIBUTION CODE

13. ABSTRACT (Maximum 200 words)

Under this program, we constructed an advanced optical phase detection, control and analysis system for space-time interferometry and optical communications. The system uses scanning interferometry to extract the phase and magnitude of serial and space-time fields. Key components include precision mechanical stages and controllers, high quality optical elements, serial and parallel receiver arrays, broadband sources, and advanced electronic control, data acquisition and analysis subsystems. We used this system to extend our previous work on space-time image capture and to systematically explore advanced phase characterization techniques. This report describes our results in using this system to characterize the SNR and information capacity of phase sensitive interferometric imaging and shows experimental evidence of super-resolved scanning using phase sensitive detection.

19970314 043

14. SUBJECT TERMS

15. NUMBER OF PAGES:
50

16. PRICE CODE

17. SECURITY CLASSIFICATION OF REPORT:
UNCLASSIFIED

18. SECURITY CLASSIFICATION OF THIS PAGE
UNCLASSIFIED

19. SECURITY CLASSIFICATION OF ABSTRACT
UNCLASSIFIED

20. LIMITATION OF ABSTRACT

ONRCHI COMPUTER V 1.0 11/94

STANDARD FORM 298 (REV 2-89)

DTIC QUALITY INSPECTED 1

INSTRUMENTATION FOR ACCURATE MEASUREMENT AND CONTROL OF OPTICAL PHASE FOR TIME AND COHERENCE DOMAIN COMMUNICATIONS AND SPACE-TIME INTERFEROMETRY

Final Technical Report

Grant Number F49620-95-1-0496

Submitted to:

Dr. Alan Craig
AFOSR/NI
DURIP Program
110 Duncan Avenue, Suite B115
Bolling AFB, DC 20332-001

Prepared by:

David J. Brady
Department of Electrical and Computer Engineering
Beckman Institute
University of Illinois at Urbana-Champaign
Urbana, IL 61801

February 6, 1997

ABSTRACT

Under this program, we constructed an advanced optical phase detection, control and analysis system for space-time interferometry and optical communications. The system uses scanning interferometry to extract the phase and magnitude of serial and space-time fields. Key components include precision mechanical stages and controllers, high quality optical elements, serial and parallel receiver arrays, broadband sources, and advanced electronic control, data acquisition and analysis subsystems. We used this system to extend our previous work on space-time image capture and to systematically explore advanced phase characterization techniques. This report describes our results in using this system to characterize the SNR and information capacity of phase sensitive interferometric imaging and shows experimental evidence of super-resolved scanning using phase sensitive detection.

I. INTRODUCTION

Increasing sophistication in the control and detection of optical fields is revolutionizing electro-optic technology. The purpose of this program was to build a well characterized interferometric space-time field analysis system to quantitatively characterize the information capacity of emerging detection systems for applications in communications, microscopy, and data storage. A space-time system uses the propagation and diffraction of fields to transform between spatial parameters and temporal or spectral parameters. Interferometers are a classic example of systems that transform spatial parameters, such as mirror position, into spectral or temporal measurements of a field. Ultra-fast pulsed lasers and optical pulse shapers have dramatically expanded the variety of space-time systems and revitalized the need for advanced serial and imaging, linear and nonlinear interferometers for phase sensitive field detection. Over the past several years, we have developed serial and imaging cross-correlating interferometers for phase sensitive field detection. Instrumentation provided under this program allowed us to systematically characterize the capabilities of these systems.

The space-time analysis system built under this program has components in four key areas: opto-mechnics, data acquisition, broadband sources and computational analysis. Under DURIP support, we integrated extra-ordinarily precisely controlled and characterized mechanical positioning systems with our existing interferometric hardware and we dramatically improved our data acquisition and computational analysis hardware. These improvements allowed us to quantitatively evaluate the information gathering potential of space-time imaging systems, as described below. We also acquired a nonlinear harmonic generating system to allow us to shift our analysis systems to key spectral ranges and we improved our existing short pulse and broad band source systems.

The second and third sections of this report detail the results obtained with the equipment supplied under this grant. Section II details the theory of interferometric cross correlation for the detection of space-time fields and describes experimental demonstrations of noise and information limits of this technique probed using the characterization system built under this program. The results of section II are presented in the refereed literature in "Noise and Information in Interferometric Cross Correlators," which has been accepted for publication in *Applied Optics*. The authors of the paper are Kent B. Hill (now at the Naval Research Laboratory), Scott A. Basinger (now at the Jet Propulsion Laboratory), and Ronald A. Stack and David J. Brady of the University of Illinois. Section III describes the results of particular experimental application of space-time imaging with interferometric cross-correlators, superresolved optical scanning. Section III includes a detailed description of the phase and amplitude characterization system built under this program and describes how this system can be used to detect subwavelength shifts in object position in interference microscopy. The results of section III have been submitted for publication in the *Journal of the Optical Society of America A* as "Superresolved optical scanning using polychromatic light," by Scott A. Basinger, Ronald A. Stack, Kent B. Hill, and David J. Brady.

II.1 Noise and information in interferometric cross correlators

Interferometric cross correlators are used to detect the amplitude and phase of optical signals in interferometric microscopy[1], ultra-fast signal characterization[2,3], dispersive spectroscopy, profilometry, coherence tomography, and time-gated 3-D imaging. The noise properties of interferometric spectrometers have previously been considered in the context of Fourier-transform spectroscopy (FTS), where the focus is on autocorrelation. Developing applications, such as interference microscopy and coherence tomography, differ from FTS in emphasizing phase sensitive detection and cross correlation. The most important difference between auto and cross correlation measurements is that while the time bandwidth product of an autocorrelation is essentially one, the time bandwidth product of a cross correlation may be large. The additional information capacity implied by this difference requires that previous studies of the noise characteristics of FTS be extended. This section describes phase sensitive cross correlation and evaluates the effect of various noise sources both theoretically and experimentally.

The information capacity of a conventional 2-D imaging system scales linearly with the space-bandwidth product, meaning that as one increases the aperture of the imaging system one expects a quadratic increase in the information capacity. In principle, the information capacity of an interferometric imaging system should be linear in the space-time bandwidth product, meaning that as one increases the temporal scan range of the interferometer one should obtain a linear increase in the information capacity. Since the noise in the cross correlation increases as the temporal aperture increases, however, the information detection capacity of a given correlator ultimately decreases as the temporal aperture increases. This means that there exists an optimal temporal aperture for a given correlator and a maximal information capacity. Analysis of these quantities is a key result of this section. The remainder of this section briefly reviews the history of FTS and dispersive FTS and motivates the work by describing some applications. Succeeding sections describe the process of interferometric cross correlation, analyze noise sources and information capacity, and present experimental results.

Two advantages have been emphasized in comparing FTS with other approaches. The Fellget or multiplex advantage is that the signal-to-noise ratio for a measurement of M spectral channels may be improved by a factor of $\sqrt{M}$ relative to grating spectrometry due to the fact that all spectral elements are measured simultaneously in FTS[4]. In FTS each spectral element is measured during the entire measurement time T rather than T/M as is done in a grating spectrometer. The Fellget advantage is obtained if the noise detected during the measurement does not increase by detecting all the spectral elements simultaneously. The Jacquinot or throughput advantage is that the light-gathering efficiency is improved compared to slit spectrometers[5]. A thorough analysis of FTS was presented by Connes in 1961[6], and noise levels in FTS have been considered by several workers since then[7–11]. Cross correlation methods analogous to the techniques discussed in this section were developed later in the 1960s, when it was shown that a sample can be placed in one arm of an interferometer to measure its wavelength dependent transmittance or reflectance[12,13]. Recent reviews of this technique, known as dispersive FTS, have been given by Birch[14] and Parker[15]. FTS has generally been used in the far infrared, where less positioning accuracy is necessary and where the multiplex advantage is significant. In the near-IR and visible ranges, FTS has no fundamental noise advantage over grating devices but still maintains the throughput advantage. The throughput advantage is of particular importance in imaging applications, where less power per channel is available and where high spectral sensitivity per unit analyzer volume is vital. As translation stage technology has improved, therefore, interferometric techniques for visible field analysis have attracted increasing interest.

Applications of interferometric cross correlators include profilometry and tomography. The phase of the field scattered from an uneven or rough surface provides information about the depth of the surface. If the surface depth of the object varies slowly, then phase-shifting techniques can be used to construct a map of the surface from the detected signal[16,17]. The resolution of these measurements is often limited by vibrations that cause uncertainties in the path delay between the reference and signal beams. Heterodyne systems can be used to compensate for these errors[18]. In white-light interferometry, an illuminating source with multiple wavelengths or a short coherence length is used to resolve sharp depth variations on a surface[19–23]. In these systems the location of the central fringe in a cross correlation determines the depth of the object from which light is reflected. In optical coherence-domain reflectometry, multiple reflections from optical components are detected[24–26]. Similar techniques which use ultrashort pulses for time-gated imaging of objects embedded in scattering media have been developed[27,28]. In optical coherence tomography, white-light sources can be used in place of pulsed sources, and the short coherence length acts as a time gate for the scattered image[29–31].

We have focused on two emerging applications of interferometric cross correlators: repetitive ultra-fast characterization and interferometric microscopy. Linear interferometers have not generally been used for ultra-short pulse characterization because linear autocorrelation yields only the power spectral density, rather than the temporal waveform of the target field. Nonlinear techniques, most notably frequency resolved optical gating[32], have been developed to overcome this problem and determine the temporal waveform of short pulses. Once one has determined the shape of a short pulse, one uses the pulse to probe some physical situation. If the bandwidth of the modified probe pulse is not substantially shifted, the temporal structure of the modified signal can be determined by linear cross correlation with a copy of the original pulse. This technique can be used to analyze extraordinarily complex space-time fields, as demonstrated recently in the detection of holographically encoded space-time images[2]. Interference microscopy expands on studies of white-light interferometry by considering modulation of the space-time structure of fields by dispersive scattering. We have shown that when form dispersion is considered, a 3-D interferometric imaging system detects more information about scattering objects than a conventional imaging system[1]. In principle, this additional information should lead to improvements in the resolution of imaging systems. As discussed in our previous work, the increase in the detected information is highly dependent on the signal-to-noise ratio (SNR) of the detection system.

The basic process of detection of complex optical fields by interferometric cross correlators is developed in Section II.2. Signal-to-noise analysis for practical systems and a discussion of the information capacity of these systems are presented in Section II.3. Experimental results are presented which demonstrate the detection of space-time fields and their noise characteristics in Section II.4.

II.2 INTERFEROMETRIC CROSS CORRELATION

It is convenient to work with the analytic signal representation of the electromagnetic field. The analytic signal corresponding to a real-valued non-monochromatic signal $u^{(r)}(t)$ with Fourier spectrum $U^{(r)}(\nu)$ is defined by doubling the positive frequency components and suppressing the negative frequency components[33,34]. Thus,

$$u(t) = 2\int_0^\infty U^{(r)}(\nu)\exp(-j2\pi\nu t)\,d\nu. \tag{1}$$

The Fourier spectrum of the analytic signal contains no negative frequency components.

The geometry of an interferometric cross correlator is shown in Fig. 1. A reference field whose analytic signal is given by $u(x,y,t)$ is split by a beamsplitter in a Michelson interferometer. In one arm of the interferometer, the field is reflected by an object whose impulse response we model as $h_o(x,y,t)$. The signal field at the output of the interferometer is then $u(x,y,t)*h_o(x,y,t)*h_1(x,y,t)$, where $*$ denotes convolution and $h_1(x,y,t)$ represents the impulse response caused by diffractive effects of the rest of the system. In the second arm of the interferometer, the reference field is reflected by a mirror on a translation stage which controls the time delay through this path and to the detector. If both paths experience the same diffractive effects from the rest of the system, the total field at the detector is given by

$$u_d(x,y,t) = u_h(x,y,t-\tau) + u_h(x,y,t) * h_o(x,y,t), \tag{2}$$

where $u_h = u * h_1$ and the time delay τ reflects the difference in the optical path length along the reference and signal interferometer arms. The detector integrates the intensity of the field over an exposure time T, and the output signal can be expressed as

$$\begin{aligned}
I(x,y,\tau) &= \int_0^T |u_d(x,y,t)|^2\, dt \\
&= \int_0^T \Big[|u_h(x,y,t)|^2 + |h_o(x,y,t) * u_h(x,y,t)|^2 \\
&\qquad + u_h^*(x,y,t+\tau)h_o(x,y,t) * u_h(x,y,t) \\
&\qquad + u_h(x,y,t+\tau)\left(h_o(x,y,t) * u_h(x,y,t)\right)^*\Big]\, dt. \qquad (3)
\end{aligned}$$

The first two terms on the right-hand side of Eq. (3) are constant with respect to τ. If T is long enough, then the last two terms contain the temporal cross correlation of the beams from each path of the interferometer. Since interferometric cross correlation is a first-order process, the contribution of the incident field to the detected temporal signal only depends on the power spectral density of the source. If the input field is spatially uniform, then the last two terms of Eq. (3) can be written as

$$\begin{aligned}
&\int_0^T u_h^*(t+\tau)h_o(x,y,t) * u_h(t)dt + c.c. \\
&\qquad = \int_0^T dt\, u_h^*(t+\tau) \int_{-\infty}^{\infty} dt'\, u_h(t-t')h_o(x,y,t') + c.c. \\
&\qquad = \int_{-\infty}^{\infty} dt'\, h_o(x,y,t') \int_0^T dt\, u_h(t+\tau)u_h(t-t') + c.c. \\
&\qquad = \int_{-\infty}^{\infty} dt'\, h_o(x,y,t')\Gamma_h(t'+\tau) + c.c., \qquad (4)
\end{aligned}$$

where *c.c.* is the complex conjugate of its preceding expression, and $\Gamma_h(\tau)$ is the self-coherence function of the optical field defined as

$$\Gamma(\tau) = \int_{-\infty}^{\infty} u(t+\tau)u^*(t)dt. \qquad (5)$$

It can be seen that the substitution of the self-coherence function in the last line of Eq. (4) is only valid if T is much longer than the duration of the impulse response and the width of $\Gamma(\tau)$. According to the Wiener-Khinchin theorem, the self-coherence function can also be expressed as the inverse Fourier transform of the power spectral density of the field:

$$\Gamma(\tau) = \int_{-\infty}^{\infty} |u(\nu)|^2 \exp(-j2\pi\nu t)d\nu. \qquad (6)$$

Thus a temporally incoherent (white-light) source will yield the same intensity as a coherent source with an equivalent power spectral density. White-light sources can have much wider bandwidths and are much less expensive than mode-locked laser sources. However, it is difficult to obtain good spatial coherence from white-light sources. Spatial coherence is necessary in order to maintain our assumption that the source can be represented as a quasi-monochromatic plane wave.

The impulse response $h_o(x, y, t)$ is recovered by taking the Fourier transform of $I(x, y, \tau)$ with respect to τ. For $\nu > 0$ and assuming that $u_h(t)$ is a stationary signal and that T is much longer than the duration of the impulse response and the correlation time of $u_h(t)$, we obtain

$$I\left(x, y, \nu\right) = \left|U_h\left(\nu\right)\right|^2 H_o\left(x, y, \nu\right), \tag{7}$$

where we make use of the fact that the negative frequency components of the analytic signals are zero. $H_o(x, y, \nu)$ can be obtained over the bandwidth of $U_h(\nu)$ by dividing Eq. (7) by $|U_h(\nu)|^2$. Given $H_o(x, y, \nu)$, we can reconstruct a bandlimited version of the object impulse response by inverse Fourier transforming. The amount of information that can be extracted from a cross-correlation measurement depends on the amount of noise superimposed on the signal. In the following section, we consider the sources of noise in interferometric cross correlators and determine the information capacity of detected signals.

II.3 SNR ANALYSIS OF INTERFEROMETRIC DETECTORS

In this section we consider the different sources of noise in a practical interferometric cross correlator and derive SNR limits which characterize this detection technique. We begin with a qualitative description of noise sources in an interferometric cross correlator. Signal noise is caused by fluctuations in the intensity of light emitted by the source or by fluctuations in the transmissive medium between the source and the detector. In an interferometer, signal noise is increased by mechanical instabilities which cause uncertainties in the path delay between the interfering beams. Quantum or shot noise arises in the photoelectric detection of light. Thermal noise adds to the signal power incident on the detector and to the the signal as the photocurrent is amplified and processed by analog electronics. Quantization error is caused by discrete thresholding of the signal during the analog-to-digital conversion process.

The relative contribution of each noise source depends on the particular system and its application. Signal noise can be reduced by using a highly stabilized source and by controlling the environment to stabilize fluctuations in the transmissive medium in the interferometer. In applications where the visibility of the interference fringes is high, the intensity of the signal varies significantly as a function of path delay, and the contribution to signal noise from inaccuracies in the path delay increases. This effect is less significant in the IR region where the intensity of the fringes varies slowly over slight changes in the path delay. However, in the visible region of the spectrum this effect must be considered. Thermal noise is significant when the photon energies of the optical signal are comparable to or less than those associated with thermal radiation. However, detectors of visible to near-IR radiation collect very little thermal radiation. CCD detectors can be obtained with 16-bit analog-to-digital converters, and the thermal noise is typically less than one bit when the detectors are cooled to low temperatures and operated at narrow electrical bandwidths. In interferometric cross correlators, the exposure time can be increased to decrease the bandwidth and reduce the effects of thermal noise. With a dynamic range of 16 bits, these detectors are ultimately limited by shot noise when detecting visible to near-IR radiation at moderate to high signal intensities and narrow bandwidths.

We now proceed with a quantitative analysis of the noise in an interferometric cross correlator. To recover the three-dimensional signal from an imaging cross correlator, a CCD array is used to detect transverse images of $I(x, y, \tau)$ at evenly spaced intervals. The time delay of the reference beam for the n^{th} sample is given by $\tau_n = n\Delta\tau$. The l, m^{th} pixel in the CCD array is centered at $(x_l, y_m) = (l\Delta x, m\Delta y)$ and has area A. Assuming that the average intensity is constant over the area of each pixel, the number of photons collected at the l, m^{th} pixel for a given reference delay is given by

$$p_{l,m,n} = \frac{\eta}{2\hbar\omega_0}\epsilon_0 c A I(x_l, y_m, \tau_n), \tag{8}$$

where ϵ_0 is the free-space permittivity (in c.g.s. units), c is the speed of light, ω_0 is the center frequency of the field, and η is the quantum efficiency of the CCD. For notational convenience, we define

$$\gamma = \frac{\eta}{2\hbar\omega_0}\epsilon_0 c A. \tag{9}$$

In practice, shot noise contributes to the number of detected photons, and the root mean square value of the shot noise at each pixel is given by $\sqrt{p_{l,m,n}}$. Although the constant terms in Eq. (3) are filtered out in the recovered cross correlation, the shot noise generated by these terms is evenly distributed over the entire spectrum of the detected signal.

The noise statistics for a given spatial channel in our system are independent of the spatial location of the channel. Therefore, the x and y dependencies of the detected signal are neglected in the following analysis. We assume that for a given path delay $n\Delta\tau$, the reference field at the plane of the detector can be written as $u(t - n\Delta\tau + \chi_n)$, where χ_n is the positioning error in the reference delay for the n^{th} sample. The number of photons detected by a given pixel in the detected image can then be written as

$$p_n = \gamma I_n = \gamma \int_0^T \left|\alpha u(t - n\Delta\tau + \chi_n) + u(t) * h_o(t)\right|^2 dt, \tag{10}$$

where α is a scaling constant used to adjust the relative intensities of the signal and reference fields.

The signal is filtered by taking discrete Fourier transforms (DFT) of the data collected at each pixel with respect to τ. The DFT is defined by

$$P_{n'} = \sum_{n=0}^{N-1} p_n \exp(j2\pi n n'/N), \tag{11}$$

where $P_{n'}$ are sampled values of the spectral power at frequency intervals $\Delta\nu = 1/N\Delta\tau$. N is taken to be even for simplicity. In calculating the statistics of $P_{n'}$, we consider $u(t)$

as a stationary random process and χ_n as a random variable. We assume that $u(t)$ is a quasi-monochromatic beam and that the variance of χ_n is much less than the mean optical period. In this case, $u(t - n\Delta\tau + \chi_n) \approx u(t - n\Delta\tau)\exp(j2\pi\nu_0\chi_n)$, where $\nu_0 = \omega_0/2\pi$. We consider first the expected value of $P_{n'}$. Assuming that χ_n is normally distributed with zero mean and variance σ_χ and that the expectation values of the reference and scattered intensities are independent of n, we find for $n' \neq 0$ that the expected value of $P_{n'}$ is

$$\begin{aligned}\langle P_{n'}\rangle = &\left\langle \gamma\alpha^* \exp\left(-2\pi^2\nu_0^2\sigma_\chi^2\right) \sum_{n=0}^{N-1} \exp\left(j2\pi n n'/N\right)\right.\\ &\left.\times \int_0^T dt \int_{-\infty}^{\infty} d\nu\, \exp\left(-j2\pi\nu t\right) u^*\left(t - n\Delta\tau\right) U\left(\nu\right) H_o\left(\nu\right)\right\rangle\\ &+ \left\langle \gamma\alpha \exp\left(-2\pi^2\nu_0^2\sigma_\chi^2\right) \sum_{n=0}^{N-1} \exp\left(j2\pi n n'/N\right)\right.\\ &\left.\times \int_0^T dt \int_{-\infty}^{\infty} d\nu\, \exp\left(-j2\pi\nu t\right) u\left(t - n\Delta\tau\right) U^*\left(-\nu\right) H_o^*\left(-\nu\right)\right\rangle, \end{aligned} \tag{12}$$

where we have expressed the convolution as an inverse Fourier transform. Assuming that T is large enough that the integration range over t can be considered infinite, we can perform this integral and sum to obtain

$$\begin{aligned}\langle P_{n'}\rangle = &\gamma\alpha^* \exp\left(-2\pi^2\nu_0^2\sigma_\chi^2\right) \int_{-\infty}^{\infty} d\nu\, \exp\left(j\pi\left(N-1\right)\left(\frac{n'}{N} - \Delta\tau\nu\right)\right)\\ &\times \frac{\sin\left(N\pi\left(\Delta\tau\nu - \frac{n'}{N}\right)\right)}{\sin\left(\pi\left(\Delta\tau\nu - \frac{n'}{N}\right)\right)} \left\langle \left|U\left(\nu\right)\right|^2\right\rangle H_o\left(\nu\right)\\ &+ \gamma\alpha \exp\left(-2\pi^2\nu_0^2\sigma_\chi^2\right) \int_{-\infty}^{\infty} d\nu\, \exp\left(j\pi\left(N-1\right)\left(\frac{n'}{N} + \Delta\tau\nu\right)\right)\\ &\times \frac{\sin\left(N\pi\left(\Delta\tau\nu + \frac{n'}{N}\right)\right)}{\sin\left(\pi\left(\Delta\tau\nu + \frac{n'}{N}\right)\right)} \left\langle \left|U\left(-\nu\right)\right|^2\right\rangle H_o^*\left(-\nu\right). \end{aligned} \tag{13}$$

$\langle P_{n'}\rangle$ is thus the convolution of the target spectrum and a comb function and is periodic in n' with period N. In the range $0 < n' < N/2$, $\langle P_{n'}\rangle$ represents $\left\langle \left|U\left(\nu\right)\right|^2\right\rangle H_o\left(\nu\right)$ to an approximate resolution of $1/N\Delta\tau$ as long as the period of the comb function is large enough to satisfy the Nyquist criterion, $\Delta\tau < \Delta\tau_N = 1/2\nu_{\max}$, where ν_{max} is the largest frequency at which $\left\langle \left|U\left(\nu\right)\right|^2\right\rangle H_o\left(\nu\right)$ is nonzero.

Noise arises in $P_{n'}$ from intensity fluctuations, shot noise, and positioning error and instability. We estimate the impact of these noise sources by calculating the variance of $P_{n'}$. Since $P_{n'}$ is a complex signal, we must calculate the variances of the real and imaginary parts separately and their joint covariance. It can be shown, however, that the covariance of the real and imaginary parts vanishes and that the variances of the real and imaginary parts are equal[34]. Therefore, it is sufficient to determine the quantity

$$\begin{aligned}\sigma_P^2 &= \left\langle |P_{n'}|^2 - \left|\langle P_{n'}\rangle^2\right|\right\rangle \\ &= \left\langle \Re\{P_{n'}\}^2 - \langle \Re\{P_{n'}\}\rangle^2\right\rangle + \left\langle \Im\{P_{n'}\}^2 - \langle \Im\{P_{n'}\}\rangle^2\right\rangle. \end{aligned} \tag{14}$$

Substitution from Eq. (11) yields

$$\sigma_P^2 = \sum_{n=0}^{N-1} \left\langle p_n^2 - \langle p_n\rangle^2\right\rangle = \sum_{n=0}^{N-1} \sigma_p^2. \tag{15}$$

The total variance in the number of detected photons can be written as[34]

$$\sigma_p^2 = \gamma\langle I_n\rangle + \gamma^2\sigma_I^2, \tag{16}$$

where the first term on the right-hand side is contributed by shot noise, and σ_I^2 is the variance in the time-average intensity caused by intensity fluctuations and positioning errors.

To evaluate Eq. (15), we have to model the statistics of I_n. We can express I_n as

$$I_n = E + \exp\left(-j2\pi\nu_0\chi_n\right) C_n + \exp\left(j2\pi\nu_0\chi_n\right) C_n^*, \tag{17}$$

where

$$E = |\alpha|^2 \int_0^T |u(t)|^2\, dt + \int_0^T |u(t) * h_o(t)|^2\, dt, \tag{18}$$

and

$$C_n = \alpha^* \int_0^T u^*(t - n\Delta\tau)\, u(t) * h_o(t)\, dt. \tag{19}$$

In neglecting the significance of temporal shifts in $u(t)$, we have assumed above that E is ergodic. In this notation the variance of the time integrated intensity is

$$
\begin{aligned}
\sigma_I^2 = \sigma_E^2 & \\
& + \left\langle \left(\exp\left(-j2\pi\nu_0\chi_n\right) C_n + \exp\left(j2\pi\nu_0\chi_n\right) C_n^* \right)^2 \right\rangle \\
& - \left\langle \exp\left(-j2\pi\nu_0\chi_n\right) C_n + \exp\left(j2\pi\nu_0\chi_n\right) C_n^* \right\rangle^2 \\
& + 2 \left\langle E \left(\exp\left(-j2\pi\nu_0\chi_n\right) C_n + \exp\left(j2\pi\nu_0\chi_n\right) C_n^* \right) \right\rangle \\
& - 2 \langle E \rangle \left\langle \left(\exp\left(-j2\pi\nu_0\chi_n\right) C_n + \exp\left(j2\pi\nu_0\chi_n\right) C_n^* \right) \right\rangle
\end{aligned} \tag{20}
$$

The first term in Eq. (20), σ_E^2, is independent of n. For quasi-monochromatic illumination, C_n and C_n^2 are weakly modulated harmonic functions of n with no dc component. These terms thus approximately vanish when summed over n. Substituting Eq. (20) in Eqs. (15) and (16), thus yields

$$
\sigma_P^2 = \gamma^2 \left[N \left(\sigma_E^2 + \frac{1}{\gamma} \langle E \rangle \right) + \sum_{n=0}^{N-1} \left\{ \left\langle |C_n|^2 \right\rangle - \left| \left\langle \exp\left(-j2\pi\nu_0\chi_n\right) \right\rangle \right|^2 \left| \langle C_n \rangle \right|^2 \right\} \right]. \tag{21}
$$

From Eq. (13), the detected signal at $n' = N\Delta\tau\nu_m$ is found to be

$$
\left| \langle P_{n'} \rangle \right| = \frac{\gamma |\alpha|}{\Delta\tau} \exp\left(-2\pi^2\nu_0^2\sigma_\chi^2\right) \left\langle \left| U\left(\nu_m\right) \right|^2 \right\rangle \left| H_o(\nu_m) \right|, \tag{22}
$$

where we neglect the effects of aliasing. If necessary, aliasing could be reduced digitally by appropriate apodization. We assume that $H_o(\nu)$ is a random function with independent real and imaginary parts. The mean of both parts is assumed to be zero and the variances are equal to σ_H. The SNR for individual signal components (i.e., the real or imaginary part of $H_o(\nu_m)$ for a particular value of m) is the ratio of $\left| \langle P_{n'} \rangle \right| / \sqrt{2}$ over the signal statistics to the variance of the real part of $P_{n'}$, which is $\sigma_P / \sqrt{2}$. Thus,

$$
\mathrm{SNR} = \frac{|\alpha| \exp\left(-2\pi^2\nu_0^2\sigma_\chi^2\right) \left\langle \left| U\left(\nu_m\right) \right|^2 \right\rangle \sigma_H}{\Delta\tau \sqrt{N \left(\sigma_E^2 + \frac{1}{\gamma} \langle E \rangle \right) + \sum_{n=0}^{N-1} \left\{ \left\langle |C_n|^2 \right\rangle - \exp\left(-2\pi^2\nu_0^2\sigma_\chi^2\right) \left| \langle C_n \rangle \right|^2 \right\}}}. \tag{23}
$$

For an unpolarized thermal source, the variance in the signal intensity is given by[34]

$$
\sigma_E^2 \approx \langle E \rangle^2 \frac{\tau_c}{2T}, \tag{24}
$$

where τ_c is the coherence time of the signal. For a white-light source $T \gg \tau_c$ and this term is negligible in comparison with the shot noise $\langle E \rangle / \gamma$. We approximate the last noise term by assuming $\langle |C_n|^2 \rangle \approx |\langle C_n \rangle|^2$ and writing

$$\sum_{n=0}^{N-1}\left\langle |C_n|^2\right\rangle \approx \left\langle \frac{1}{\Delta\tau}\int_{-N\Delta\tau/2}^{N\Delta\tau/2} dt\,|C_n|^2\right\rangle . \tag{25}$$

Parseval's theorem states that in the limit $N\Delta t \rightarrow \infty$,

$$\int_{-\infty}^{\infty} dt\,|C_n|^2 = \int_{-\infty}^{\infty} d\nu\, |\mathcal{F}\{C_n\}|^2 , \tag{26}$$

where $\mathcal{F}\{\cdot\}$ is the Fourier transform operator. Using the convolution theorem, we can write

$$\mathcal{F}\{C_n\} = \alpha^* |U(\nu)|^2 H_o(\nu). \tag{27}$$

Therefore,

$$\int_{-\infty}^{\infty} dt\,|C_n|^2 = |\alpha|^2 \int_{-\infty}^{\infty} d\nu\, |U(\nu)|^4 |H_o(\nu)|^2 . \tag{28}$$

Substituting this expression into Eq. (25) and taking the average, we obtain

$$\sum_{n=0}^{N-1}\left\langle |C_n|^2\right\rangle \approx \frac{|\alpha|^2 \nu_B}{\Delta\tau}\left\langle |U(\nu_0)|^2\right\rangle^2 \sigma_H^2 , \tag{29}$$

where ν_B is the bandwidth of the source.

We wish to calculate the SNR as a function of the various signal parameters for a fixed total detected energy per exposure. The total energy that can be detected in a single exposure by a pixel on a CCD is limited by its well capacity P_s, or the number of photogenerated electrons that saturates the detected signal. If the duration of the signal is long compared to τ_c, then the visibility of the signal fringes is weak and it can be assumed that the dc intensity dominates the signal. In this case,

$$\langle E\rangle \approx \frac{P_s}{\gamma}. \tag{30}$$

Applying Parseval's theorem to Eq. (18) we obtain

$$\left\langle |U(\nu_0)|^2\right\rangle = \frac{\langle E\rangle}{\nu_B\left(|\alpha|^2 + \sigma_H^2\right)}. \tag{31}$$

The SNR for frequencies within the bandwidth of the source can be estimated by setting $\nu_m = \nu_0$. Substituting Eqs. (29)-(31) into Eq. (23), we find that the SNR is maximized when $|\alpha|^2 = \sigma_H^2$, and we obtain

$$\mathrm{SNR} = \frac{\exp\left(-2\pi^2\nu_0^2\sigma_\chi^2\right)}{\sqrt{\frac{4(\nu_B\Delta\tau N)^2}{P_s N} + \frac{(\nu_B\Delta\tau N)}{N}\left[1 - \exp\left(-2\pi^2\nu_0^2\sigma_\chi^2\right)\right]}}. \tag{32}$$

For a fixed sampling width $\Delta\tau$ it can be seen that increasing N causes the SNR to decrease, this results from letting more noise into the same spectral window. However, for a fixed measurement duration (the product of $\Delta\tau N$), increasing N causes the expected $\propto \sqrt{N}$ increase of the SNR. One may also improve the SNR by increasing P_s or the dynamic range of the CCD camera used. To increase P_s, the well capacity of the CCD must be improved or multiple exposures must be collected for each measurement. In Fig. 2, the SNR is plotted as a function of the variance in the path delay to demonstrate the effects of these methods for increasing the SNR. To calculate the SNR plotted in Figs. 2-4, the source was assumed to have a 25 nm bandwidth centered on 570 nm. In Fig. 2(a), the SNR is plotted for a signal that is sampled at the Nyquist rate with $N = 10^4$ and $P_s = 5 \times 10^5$. These parameters are typical for the experimental system described in Section II.4. For Fig. 2(b), the signal is sampled at twice the Nyquist rate with N doubled to sample the same signal duration and P_s is unchanged. It can be seen that the SNR increases as long as the error in the path delay is small. This corresponds to the regime in which shot noise dominates. When σ_χ is large, noise caused by the positioning error dominates and the SNR does not increase significantly. For Fig. 2(c), the signal is sampled at the Nyquist rate with P_s doubled and N unchanged. In this case, it can be seen that the SNR improves for larger values of σ_χ. In both methods for improving the SNR, the total energy collected during the measurement was doubled. This accounts for a decrease in the shot noise since shot noise scales with the square root of the number of photons detected. If P_s is increased by taking multiple exposures, it is assumed that the path delay remains constant during all of the exposures.

In Fig. 3, the SNR is plotted as a function of N for two values of σ_χ. Nyquist sampling is assumed so that N corresponds to the signal duration, and $P_s = 5 \times 10^5$. When the duration of the signal is long, shot noise dominates due to the large dc component in the detected signal and the positioning error has little effect on the SNR. The positioning error is more significant for shorter signals because the amplitude of the fringes is greater; therefore, small errors in the path delay cause significant errors in the detected signal. The transition between regimes in which shot noise dominates and positioning error dominates can be seen in Fig. 4, where the SNR (normalized to its maximum) is plotted as a function of σ_X for several values of N. Nyquist sampling and $P_s = 5 \times 10^5$ are assumed. It can be seen that for signal durations longer than 10^5 periods (approximately 100 ps), the positioning error is only significant when it is greater than 1% of the wavelength. For shorter signals, smaller positioning errors become much more significant.

The model that we have derived for the SNR in interferometric cross correlators provides an understanding of the limitations of these systems. Positioning errors and mechanical instabilities must be carefully avoided when ultrafast signals are detected. To minimize the effects of shot noise, the energy collected during a measurement should be made as large as possible.

From the SNR we can also estimate the information capacity of an interferometric cross correlator. Let SNR_{min} be the minimum SNR below which any information is lost in the noise. The total information capacity is then

$$H = \nu_B T \log_2 \frac{\text{SNR}}{\text{SNR}_{\text{min}}}, \tag{33}$$

where $T = N\Delta\tau$ is the total duration of the measurement. Figure 5 shows the information capacity versus T for $\lambda_0 = 566$ nm, $\sigma_X = 6$ nm, $P_S = 500,000$, $\nu_B = 24$ THz, $\Delta\tau = 100$ nm, and $\text{SNR}_{\text{min}} = 80$. Note that the information capacity has a maximum at a certain signal duration and decreases as the length of the signal increases. Thus, increasing the information content of the signal may actually decrease the detected information.

II.4 EXPERIMENTAL RESULTS

To demonstrate the detection of space–time fields, we detected the field reflected from a thick scattering sample by using the arrangement of Fig. 1. A beam from a spatially coherent white-light source was the input to an imaging interferometric cross correlator as described in Section II.2. A point fluorescent source similar to that developed by Liu et al.[35] was used to obtain a broad bandwidth and good spatial coherence. A low numerical aperture lens focused the image scattered from the object with high depth of field onto a scientific-grade, cooled CCD with 16-bit dynamic range (Princeton Instruments) at the output of the interferometer. An electro-motive translator (MPB) with external feedback from an inductive position sensor (Kaman Instrumentation) was used in combination with a linear translation stage (Aerotech) to control the path delay of the reference beam. Subwavelength steps with $\approx$ 20-nm absolute resolution were obtained over 40-μm intervals, and the linear stage was translated by 40 μm at the end of each interval. Neutral density filters F_1, F_2 and F_3 equalize the total energy collected from each arm of the interferometer and adjusted the total energy incident on the CCD. By placing a filter in each arm of the interferometer, the dispersion caused by the filters was compensated. Reflections from the faces of the filters and the sample were separated from the image by slightly tilting these surfaces. A PC controlled the experiment and stored the data collected from the CCD during the cross correlation.

The noise characteristics of this detection system were determined by statistical analysis of a series of autocorrelation measurements. A total of 99 autocorrelations were performed with data collected from 121 pixels in each measurement. The imaging lens was removed during these measurements to yield a uniform beam intensity over the area of these pixels. The SNR ($\langle P_{n'}\rangle/\sigma_P$) calculated from these data is plotted in Fig. 6. In Fig. 6(a), the statistics were calculated using the data from each of the 121 pixels in a single measurement. In a single measurement, the noise due to positioning errors and mechanical instabilities is identical for each pixel. Therefore, only the noise due to source intensity fluctuations, quantum noise, thermal noise and electrical noise is included in the SNR plotted in Fig. 6(a). The maximum SNR in this plot is approximately 250. In Fig. 6(b), the noise due to all effects was included by calculating the statistics of the spectral data collected from a single pixel over all of the measurements. In this case, the SNR was reduced to about 200.

It appears that the primary source of noise in our experiments was shot noise. The average number of photoelectrons detected in each data point was $\langle p_n \rangle \approx 2.2 \times 10^5$, and the number of samples taken was $N = 309$. By substituting our experimental parameters into Eq. (32), the theoretical value of the SNR is found to be approximately 900 for no positioning error. With a positioning error of 1% of the wavelength, the theoretical SNR drops to about 180. To improve the SNR, it is necessary to increase $\langle p_n \rangle$; however, the saturation level for our CCD is 5×10^5 photoelectrons. Averaging several frames collected by the CCD would reduce the effects of shot noise, but the time required for experiments would increase proportionately. In this case, positioning errors would have a greater effect unless the path delay can be held constant during the time required to average several frames.

Systematic errors in the data collected during these experiments were eliminated by manipulating the data to compensate for the errors. Each measurement lasted approximately 5 min, and the total time required to perform 99 measurements was almost 8 h. Because the beam intensity was not perfectly uniform over the area of the pixels used to collect the data, and because the average intensity of the source varied from one measurement to the next, the data from each pixel in each measurement was normalized to have zero mean and unity standard deviation. Furthermore, because slowly varying temperature fluctuations during the experiments caused the optical path difference to change from one measurement to the next, the spectrum in each measurement was multiplied by a phase factor to compensate for the corresponding time shift in the autocorrelation.

To experimentally verify the theoretical analysis of the SNR as a function of positioning error would require several thousand measurements, with intentional positioning noise added to the reference mirror sampling positions. However, this may not yield satisfactory results due to the inherent positioning error already contained in the system. As an alternative, we took one large set of highly oversampled data by moving the reference mirror in step sizes of 20 nm. Again, we collected data from 121 pixels. In addition, we added a scheme to interferometrically detect the optical path difference between the reference mirror and the object mirror to less than 1 nm over the full range of motion of the reference mirror (4 inches). This scheme uses a reference laser beam (Spectra Physics frequency stabilized HeNe) which is placed slightly above and parallel to the signal beam. The spatial fringe pattern produced from this HeNe is then captured with the CCD array and Fourier transformed to extract the phase. By maintaining a careful history of the HeNe phase, the absolute reference mirror position can be calculated. From this real oversampled data set, we then simulated data sets with various positioning errors. Gaussian random variables, with a standard deviation of the desired positioning error, were added to uniformly sampled positions and the intensity was then interpolated at these positions from the real data set. Figure 7 shows the results for three different values of the total number of samples taken N. In each case, the total length of each measurement T was held constant, so that a greater value of N corresponds to a higher sampling density, which is why the SNR increases with N. As a comparison, the dashed lines show the same corresponding calculation for the SNR versus positioning error as determined by Eq. 32.

For the measurement of 3-D cross correlations, a scattering sample was made by adding 5-μm alumina polishing powder to a transparent epoxy (Epo-Tek 301). The epoxy was then poured between two microscope cover slides and allowed to harden. The thickness of the sample was 4 mm, and the cover slides were 150-μm thick. A cross correlation of the field scattered from this sample was measured by collecting 242 μm × 242 μm images on the CCD (11 × 11 pixels) at a rate of approximately four samples per fringe as the reference delay τ was increased. Because of the difficulty in plotting 3-D data, density plots of only three 2-D slices of the data are shown in Fig. 8. The drawing at the top of the figure shows the locations of the 2-D slices that are plotted below it. For clarity, and to reduce the amount of data to display, only the first 5.6 ps of the scattered field was detected. A total of 10,752 images were collected over this range. The DFT of the data collected from each pixel was calculated, and the inverse DFT of 350 points centered at the fringe frequency provided the filtered data shown. At $\tau \approx 0.2$ ps, the light scattered from the first surface of the sample appears, and the tilt of this surface can be seen. No further scattering can be seen until $\tau > 1.52$ ps, which corresponds to the thickness of the glass cover slide. The data collected from one pixel in the image is shown in Fig. 9(a). The DFT and the amplitude of the filtered data for this pixel are plotted in Figs. 9(a) and (b), respectively.

II.5 CONCLUSION

We have shown that interferometric cross correlators can be used to detect complex space–time fields. Because an interferometric cross correlation depends only on the power spectral density of the source, the impulse response of an object can be determined using simple white-light sources. To recover the phase of the signal, sampling of the cross correlation at the Nyquist rate must be performed. In the visible region, the main sources of noise in interferometric cross correlators are shot noise and inaccuracies in the time delay of the reference field. The SNR in these systems decreases exponentially with the variance of the error in the path delay and is scaled by a factor of $1/\sqrt{N}$, where N is proportional to the length of the signal. We have developed hardware for an interferometric cross-correlation system, and the SNR achieved in this system is approximately 200.

REFERENCES

1. S. A. Basinger, E. Michielssen, and D. J. Brady, "Degrees of freedom of polychromatic images," J. Opt. Soc. Am. A **12,** 704 (1995).
2. K. B. Hill, K. G. Purchase, and D. J. Brady, "Pulsed-image generation and detection," Opt. Lett. **20,** 1201 (1995).
3. K. G. Purchase and D. J. Brady, "Time-of-flight cross correlation on a detector array for ultrafast packet detection," Opt. Lett. **18,** 2129 (1993).
4. P. Fellgett, J. Phys. Radium **19,** 187 (1958).
5. P. Jacquinot, 17e Congres GAMS, 25 (1954).
6. J. Connes, Rev. Opt. **40,** 45, 116, 171, and 231 (1961).
7. H. Sakai, "Consideration of the signal-to-noise ratio in Fourier spectroscopy," in *Aspen International Conference on Fourier Spectroscopy,* 19 (1970).
8. E. E. Bell and R. B. Sanderson, "Spectral errors resulting from random sampling-position errors in Fourier transform spectroscopy," Appl. Opt. **11,** 688 (1972).
9. J. W. Flemming, "Noise levels in broad band Fourier transform absorption spectrometry," Infrared Phys. **17,** 263 (1977).
10. R. R. Treffers, "Signal-to-noise ratio in Fourier spectroscopy," Appl. Opt. **16,** 3103 (1977).
11. R. Meynart, "Sampling jitter in Fourier-transform spectrometers: spectral broadening and noise effects," Appl. Opt. **31,** 6383 (1992).
12. E. E. Bell, "Measurement of the far infrared optical properties of solids with a Michelson interferometer used in the asymmetric mode: part I, mathematical formulation," Infrared Phys. **6,** 57 (1966).

13. J. Chamberlain, J. E. Gibbs, and H. A. Gebbie, "The determination of refractive index spectra by Fourier spectrometry," Infrared Phys. **9,** 185 (1969).

14. J. R. Birch, "Dispersive Fourier transform spectroscopy," Mikrochim. Acta **111,** 105 (1987).

15. T. J. Parker, "Dispersive Fourier transform spectroscopy," Contemp. Phys. **31,** 335 (1990).

16. J. C. Wyant, C. L. Koliopoulos, B. Bhushan, and D. Basila, "Development of a three-dimensional noncontact digital optical profiler," J. Tribol. **108,** 2 (1986).

17. D. P. Hand, T. A. Carolan, J. S. Barton, and J. D. C. Jones, "Profile measurement of optically rough surfaces by fiber-optic interferometry," Opt. Lett. **18,** 1361 (1993).

18. M. J. Offside and M. G. Somekh, "Interferometric scanning optical microscope for surface characterization," Appl. Opt. **31,** 6772 (1992).

19. Y. N. Ning, K. T. V. Grattan, and A. W. Palmer, "Fibre-optic interferometric systems using low-coherence light sources," Sensors Actuators A **30,** 181 (1992).

20. R. Dändliker, E. Zimmermann, and G. Frosio, "Electronically scanned white-light interferometry: a novel noise-resistant signal processing," Opt. Lett. **17,** 679 (1992).

21. P. Sandoz and G. Tribillon, "Profilometry by zero-order interference fringe identification," J. Mod. Opt. **40,** 1691 (1993).

22. P. de Groot and L. Deck, "Three-dimensional imaging by sub-Nyquist sampling of white-light interferograms," Opt. Lett. **18,** 1462 (1993).

23. D. N. Wang, Y. N. Ning, K. T. V. Grattan, A. W. Palmer, and K. Weir, "Characteristics of synthesized light sources for white-light interferometric systems," Opt. Lett. **18,** 1884 (1993).

24. R. C. Youngquist, S. Carr, and D. E. N. Davies, "Optical coherence-domain reflectom-

etry: a new optical evaluation technique," Opt. Lett. **12,** 158 (1987).

25. K. Takada, I. Yokohama, K. Chida, and J. Noda, "New measurement system using a swept modulation frequency technique," Appl. Opt. **26,** 1603, 1987.

26. B. L. Danielson and C. D. Whittenberg, "Guided-wave reflectometry with micrometer resolution," Appl. Opt. **26,** 2836 (1987).

27. K. G. Spears, J. Serafin, and N. H. Abramson, "Chrono-coherent imaging for medicine," IEEE Trans. Biomed. Eng. **36,** 1210 (1989).

28. H. Chen, Y. Chen, D. Dillworth, E. Leith, J. Lopez, and J. Valdmanis, "Two-dimensional imaging through diffusing media using 150-fs gated electronic holography techniques," Opt. Lett. **16,** 487 (1991).

29. D. Huang, E. A. Swanson, C. P. Lin, J. S. Schuman, W. G. Stinson, W. Chang, M. R. Hee, T. Flotte, K. Gregory, C. A. Puliafito, and J. G. Fujimoto, "Optical coherence tomography," Science **254,** 1178 (1991).

30. H.-P. Chiang, W.-S. Chang, and J. Wang, "Imaging through random scattering media by using cw broadband interferometry," Opt. Lett. **18,** 546 (1993).

31. J. A. Izatt, M. R. Hee, G. M. Owen, E. A. Swanson, and J. G. Fujimoto, "Optical coherence microscopy in scattering media," Opt. Lett. **19,** 590 (1994).

32. D. J. Kane and R. Trebino, "Single-shot measurement of the intensity and phase of an arbitrary ultrashort pulse by using frequency-resolved optical gating," Opt. Lett. **18,** 823 (1993).

33. M. Born and E. Wolf, *Principles of Optics* (Pergamon, London, 1980).

34. J. W. Goodman, *Statistical Optics* (John Wiley & Sons, Inc., New York, 1985).

35. H.-H. Liu, P.-H. Cheng, and J. Wang, "Spatially coherent white-light interferometer based on a point fluorescent source," Opt. Lett. **18,** 678 (1993).

FIGURES

Fig. 1. Experimental setup for detecting the impulse response of a thick scattering object.

Fig. 2. SNR vs. path delay error. (a) $N = 10^4$, $\Delta\tau = \Delta\tau_N$, and $P_s = 5 \times 10^5$. (b) $N = 2 \times 10^4$, $\Delta\tau = \Delta\tau_N/2$, and $P_s = 5 \times 10^5$. (c) $N = 10^4$, $\Delta\tau = \Delta\tau_N$, and $P_s = 10^6$.

Fig. 3. SNR vs. signal duration for two values of positioning error.

Fig. 4. Normalized SNR vs. positioning error for different signal durations.

Fig. 5. Information capacity as a function of signal duration for $\lambda_0 = 566$ nm, $\sigma_\chi = 6$ nm, $P_S = 500,000$, $\nu_B = 24$ THz, $\Delta\tau = 100$ nm, and $\mathrm{SNR}_{\mathrm{min}} = 80$.

Fig. 6. SNR for experimental cross-correlation system. (a) SNR without positioning and mechanical errors. (b) Total SNR. The dashed line shows the shape of the mean spectrum with arbitrary scale.

Fig. 7. Experimentally determined SNR versus positioning error for three different sampling densities and the corresponding theoretical calculations (dashed lines).

Fig. 8. Density plots of the space–time field scattered from a thick scattering sample.

Fig. 9. Cross-correlation data from one pixel in the space–time field scattered from a thick scattering sample. (a) Raw data. (b) DFT of raw data. (c) Amplitude of the filtered cross correlation.

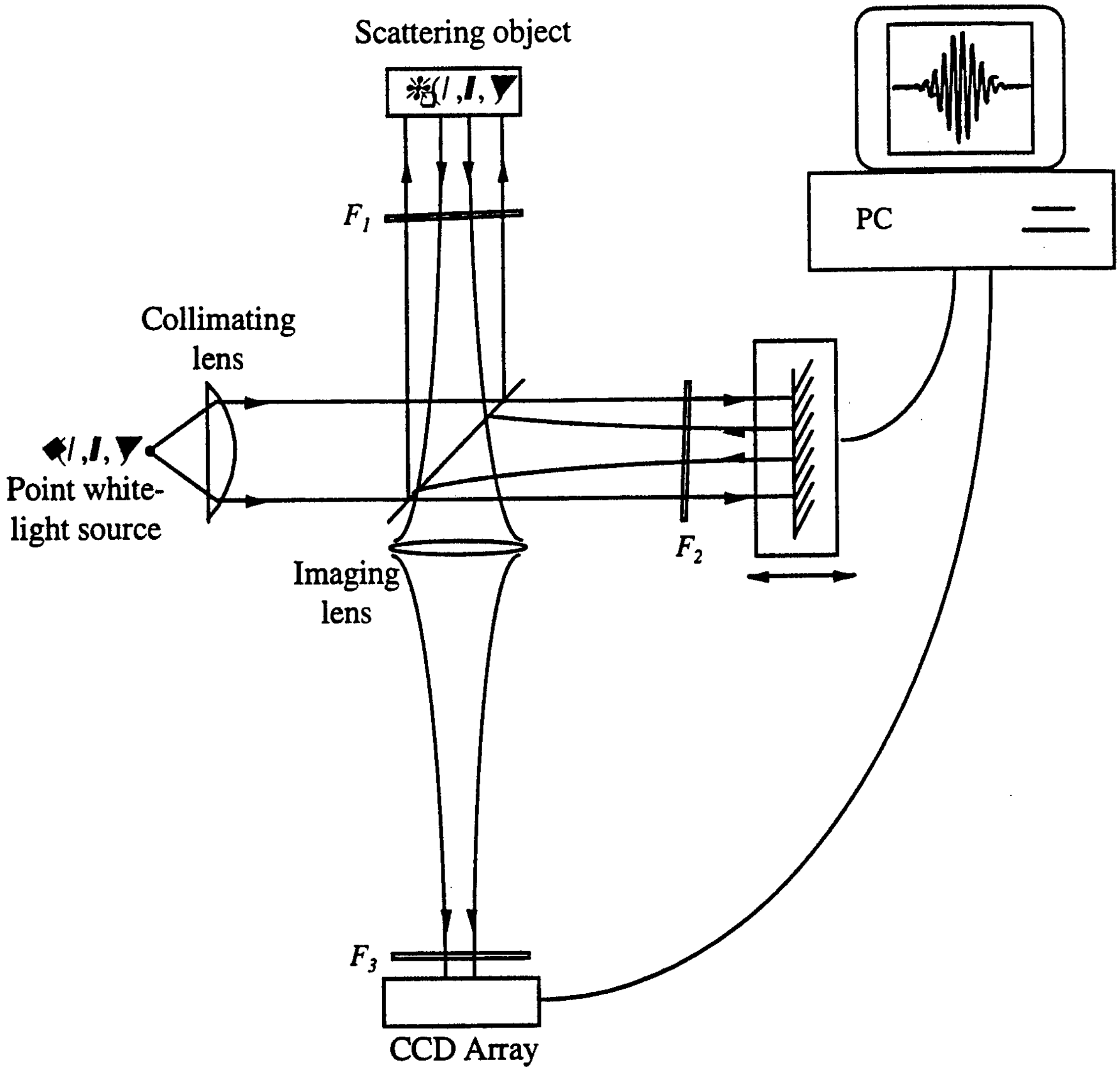

Fig. 1. Experimental setup for detecting the impulse response of a thick scattering object.

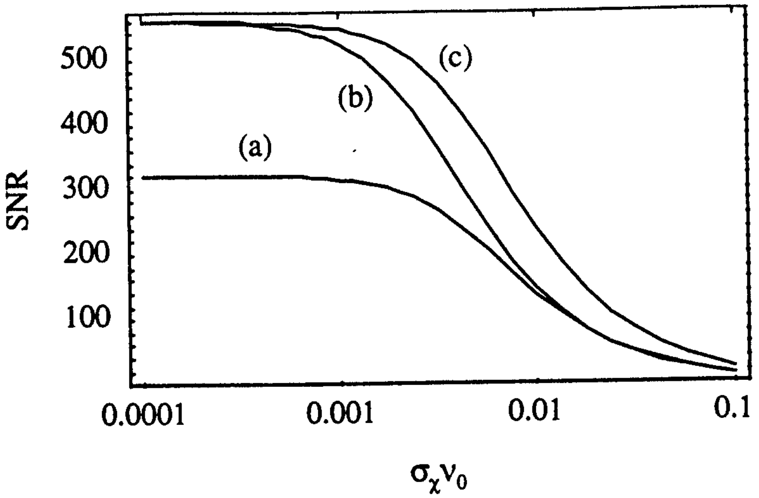

Fig. 2. SNR vs. path delay error. (a) $N = 10^4$, $\Delta\tau = \Delta\tau_N$, and $P_s = 5 \times 10^5$. (b) $N = 2 \times 10^4$, $\Delta\tau = \Delta\tau_N/2$, and $P_s = 5 \times 10^5$. (c) $N = 10^4$, $\Delta\tau = \Delta\tau_N$, and $P_s = 10^6$.

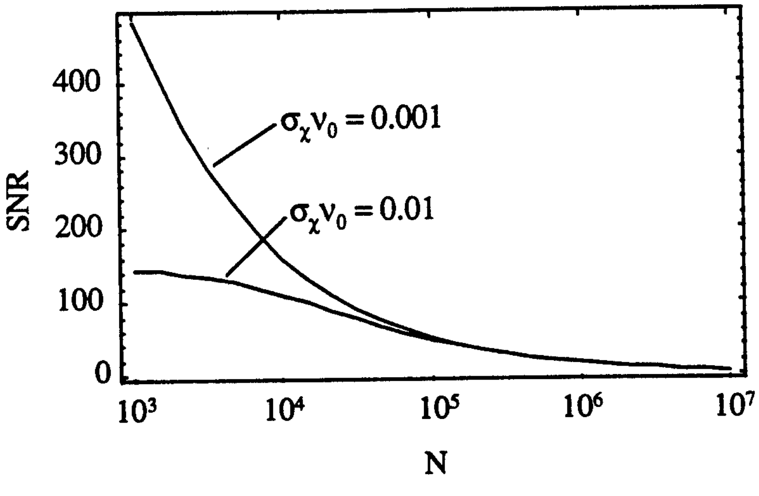

Fig. 3. SNR vs. signal duration for two values of positioning error.

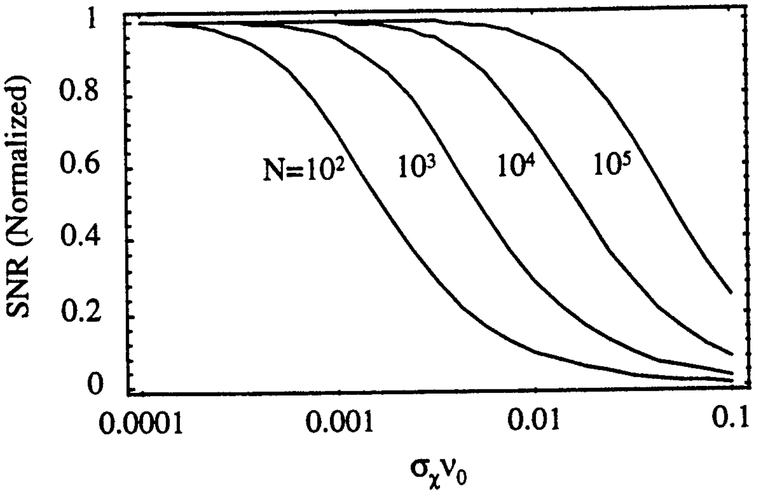

Fig. 4. Normalized SNR vs. positioning error for different signal durations.

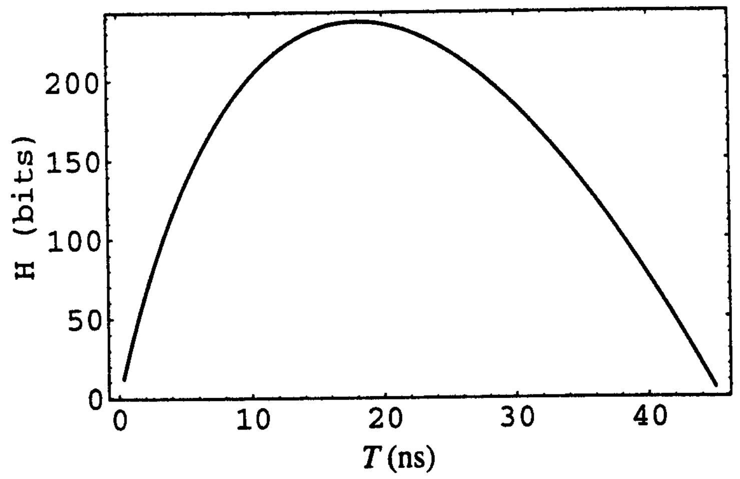

Fig. 5. Information capacity as a function of signal duration for $\lambda_0 = 566$ nm, $\sigma_\chi = 6$ nm, $P_S = 500,000$, $\nu_B = 24$ THz, $\Delta\tau = 100$ nm, and $\text{SNR}_{\text{min}} = 80$.

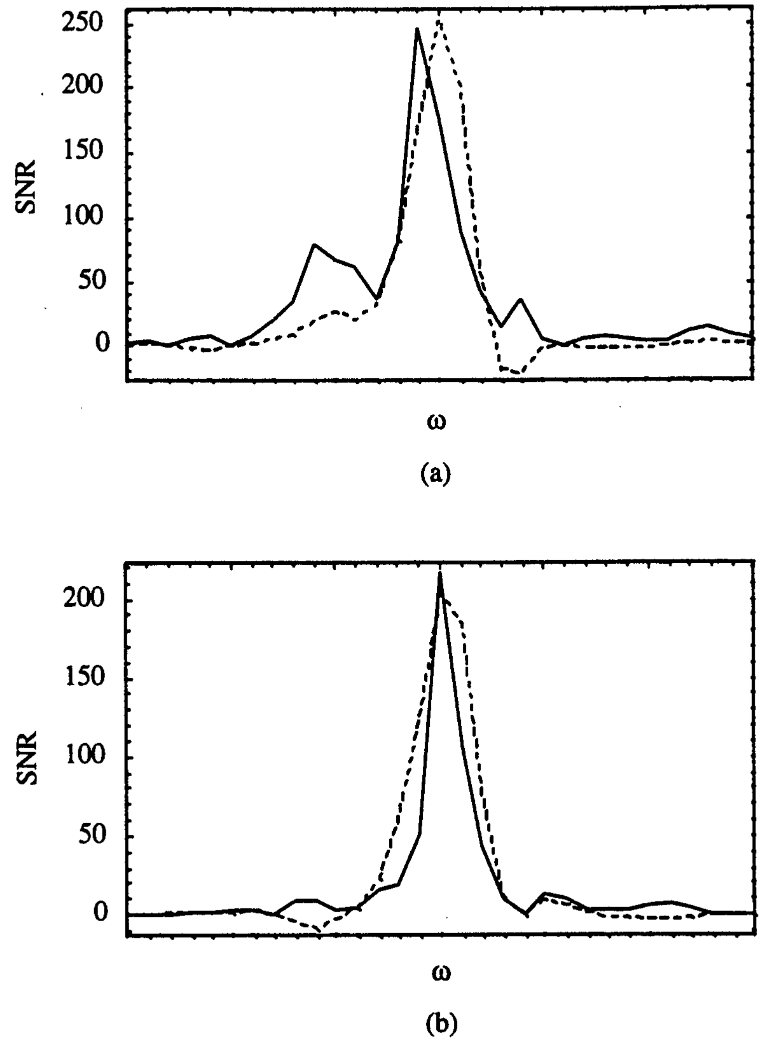

Fig. 6. SNR for experimental cross-correlation system. (a) SNR without positioning and mechanical errors. (b) Total SNR. The dashed line shows the shape of the mean spectrum with arbitrary scale.

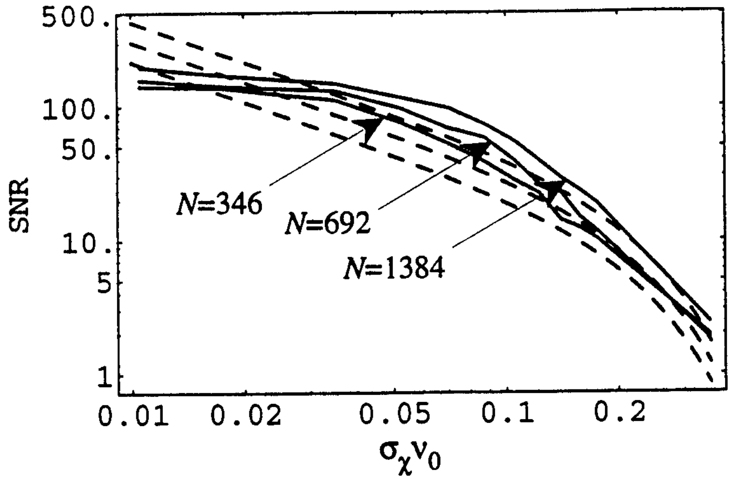

Fig. 7. Experimentally determined SNR versus positioning error for three different sampling densities and the corresponding theoretical calculations (dashed lines).

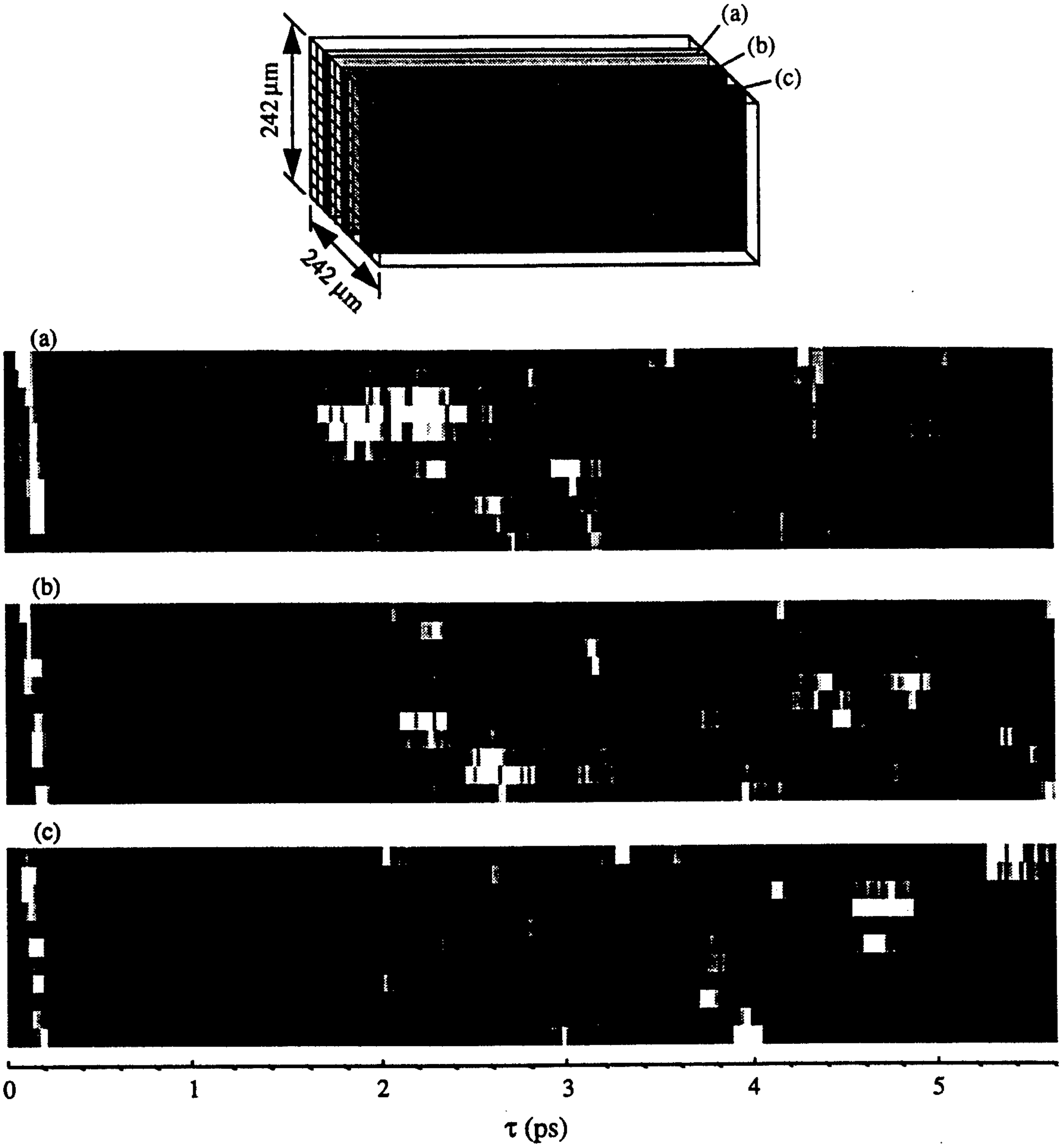

Fig. 8. Density plots of the space–time field scattered from a thick scattering sample.

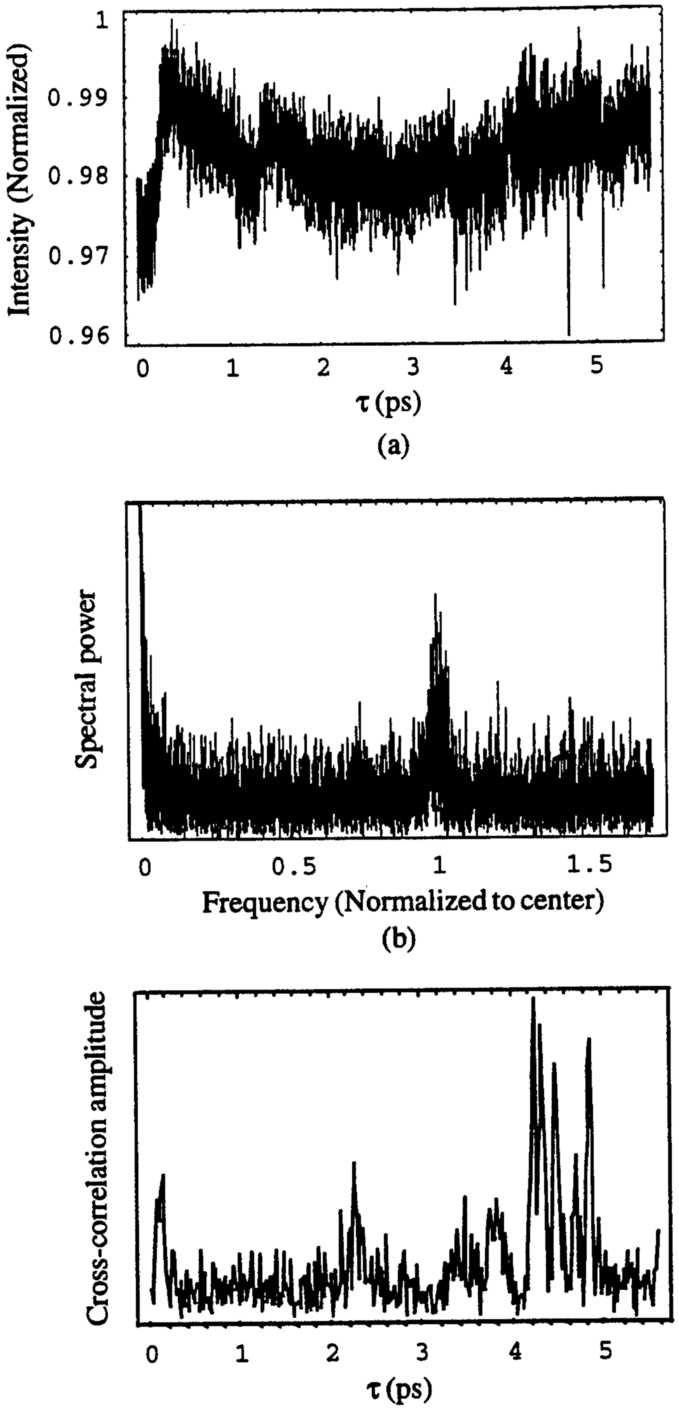

(a)

(b)

(c)

Fig. 9. Cross-correlation data from one pixel in the space–time field scattered from a thick scattering sample. (a) Raw data. (b) DFT of raw data. (c) Amplitude of the filtered cross correlation.

The concept of "resolution" is based on the observation that a given system cannot distinguish between different objects if the differences are on too small of a spatial scale. Translation is among the simplest techniques for creating different objects. A classical imaging system cannot distinguish between an object and the same object shifted by an amount less than the classical resolution limit of one-half the center wavelength of the probing light. The resolution limit of an interferometric imaging system is discussed below. The goal of this section is to show that the resolution limit of an interferometric imaging system using polychromatic light can exceed that of a classical imaging system. We do this by demonstrating that our interferometric imaging system can detect much smaller transverse shifts in object position than its classical counterpart could.

Our expectation that an interferometric imaging system should yield higher resolution can be understood by considering how information is encoded in imaging and tomographic systems. The "object" in such systems is a passive spatial structure which scatters probe or ambient light into the imaging system. The amplitude and phase of the scattered light vary as functions of spatial structure and composition of the object. The system collects this scattered light and uses it to reconstruct an "image," which is a map of the spatial and spectral distribution of the scattered field in the neighborhood of the object. The structure of the object is inferred by analogy with the image. In a classical imaging system, the relative phase of different temporal frequency components is lost on detection. The relative phase is particularly important in determining the effects of form dispersion which can be used for subwavelength detection. A high spatial frequency structure in an object, while not directly observable in its effect on the intensity of the scattered field, can shift the phase of spectral and spatial components in the scattered field. These phase shifts can be detected by considering the relative phases between the different spectral components in the scattered field. Interferometric detection is necessary to detect these relative phases.

Since the scattering processes associated with imaging are linear, it is not necessary to detect the temporal characteristics of the scattered field to obtain the relative phases between different frequency components. These relative phases can be determined by measuring the impulse response of the scattering process. By "impulse response" we mean the field scattered when the object is illuminated by an impulse in the spatial frequency and temporal frequency domains, e.g. a plane wave temporal impulse. In practice, it is not possible to generate or detect the complete impulse response, but a temporally and spatially band-limited version can be detected interferometrically using a broadband illumination source. The use of a Michelson interferometer to determine the impulse response of a scattering object is discussed in Ref. [5]. Using this technique, one should be able to increase the amount of information detected from an object by increasing the temporal extent of the impulse response measured. This, in turn, increases the resolution of the system. However, there is a limit to the amount of information that one can detect interferometrically. As discussed in Ref. [1], the signal-to-noise ratio (SNR) of an interferometric system limits the amount of information one can extract from a measured impulse response. Thus, the resolution limit of an interferometric imaging system is bounded by the SNR of the system. The SNR of the system described here is characterized in Ref. [5]

In this section, we describe experimental results confirming that interferometric imaging of a scattered polychromatic optical field can be used to detect superresolved spatial structures. Section 2 discusses the data analysis protocol underlying our experiments. As mentioned above, inversion of 3-D data collected by our interferometric imaging system to obtain images is beyond our current capability. The data analysis protocol is the model we use to distinguish scattering data collected for different object positions. Section 3 describes the experimental system and general procedure used to collect scattering data. Finally, Section 4 presents the experimental results.

III.2. ANALYSIS PROTOCOL

In this section, the process of analyzing data collected with our interferometric cross-correlator is discussed. The purpose of our analysis is to discriminate between data sets collected at several different object positions. To gain an understanding of the principles and motivation behind our analysis, several aspects of our system and data collection procedure must be explained. First, the motivation as to the type of data taken is discussed and then the general method of data acquisition is described. Finally, we show how the data is processed to extract features and measure object position.

As stated in Section 1, "classical" imaging systems measure the time-averaged intensity of an optical field, thus losing degrees of freedom associated with the temporal structure of the field. Ref. [1] argues that the temporal degrees of freedom that are encoded in the phase spectrum of the scattered optical field need to be recovered in order to resolve a subwavelength spatial structure. While the information received by independent spatial and/or spectral channels is not completely independent, some information associated with a subwavelength spatial structure is recovered by analyzing the ensemble of data captured from the phase spectrum of the scattered optical field over a spatially separated array of detector channels. There is no direct linear mapping between this information and the spatial structure of an object's surface. Since the information received in different channels is not independent, doubling the number of spatial channels or doubling the number of spectral components does not necessarily double the information recovered. The inter-dependence of the data and the lack of a linear mapping make image construction from polychromatic data extremely challenging.

For our analysis, we simplify the problem considerably by attempting not to form an image of an object, but only to distinguish between several different object positions. This is a simpler task, since we can employ statistical methods on this data to find correlations among different object positions. For example, assume that one has several sets of phase spectrum data from one position, and several more sets from another position. If we can select one set from the ensemble and determine which object position it came from, we have succeeded in demonstrating that our system is capable of subwavelength resolution.

The statistical correlations we seek rely on data sets containing the relative phases between different spectral components of the scattered field over many spatial channels. With an interferometer we perform a cross-correlation that results in an intensity at the detector for the n_{th} sample with the following form,

$$I_n(x,y) = \int_0^T u_h(x,y,t-n\delta\tau) + u_h(x,y,t) * h_o(x,y,t) \cdot dt \,. \tag{1}$$

The function $u_h(x, y, t)$ is the impulse response of the source, and $h_o(x, y, t)$ is the impulse response of the object. The variable $\delta\tau$ is the temporal sampling width and '*' represents convolution. Note that x and y are also discrete in the sense that they correspond to individual spatial channels (pixels) on the detector. This set of data $I_n(x, y)$, $n = 1,\ldots,N$, where N is the total number of samples, is not particularly useful. However, in Ref. [5] it is shown that a Fourier transformation of this data set can be used to obtain the transfer function $H_o(x, y, \nu)$ of the object. More specifically, performing a fast Fourier transform (FFT) on $I_n(x, y)$ with respect to n, results in the object transfer function times the power spectrum of the source,

$$\mathcal{I}_n(x,y) = \left| U_h(x,y,\frac{N}{n\delta\tau}) \right|^2 H_o(x,y,\frac{N}{n\delta\tau}) \,. \tag{2}$$

Given that the power spectrum of the source is a known quantity, it can be divided out leaving only the transfer function. Since the object transfer function is the same as the phase and amplitude spectrum of the object, a Fourier transformation of the cross-correlation data will give the relative phase information form dispersion necessitates. Note that the object transfer function times the power spectrum of the source will be referred to from this point as the transfer function since the power spectrum term does not enter into our statistical analysis.

An imaging interferometric cross-correlator consists of the following: a point white-light source which is collimated and used to probe or image the object in question, a Michelson interferometer which allows us to interfere a reference drawn from the probe light with light reflected from the object, and a detector (charged coupled device or CCD) array which captures the interference pattern. An interferometer performs the cross-correlation by adjusting the distance traveled by the reference beam. The difference between distance traveled by the reference beam and the distance traveled by the object beam is called the optical path difference (OPD). Scanning the OPD throughout the entire range where an interference pattern can be detected while sampling the intensity over several spatial channels results in the set of cross-correlation data. The range of the OPD is chosen to cover the temporal extent of the band-limited object signal, while the spacing is chosen such that the sampling rate is close to the Nyquist limit of the temporal interference fringes. This cross-correlation data is collected numerous times for several different object positions.

Our statistical analysis consists of reducing the large amount of data collected to a small set of averaged parameters, a set for each object position. Comparing the absolute value of the difference between the average set of parameters for a particular position j to an individual set of parameters for a particular position i yields a number which reveals how well the data at position i matches the ensemble of data sets taken at a position j. Determining when this number is a minimum will indicates at which position this data was taken (*i.e.* when $i = j$.) A detailed description of this analysis follows.

The cross-correlation data is interpolated to evenly sampled points using accurately measured OPD values. This is done since our system's ability to accurately measure the OPD is better than its ability to control the OPD or to position the reference mirror. Interpolating to evenly spaced sample points greatly simplifies the task of performing a Fourier transform on the data, since its allows an FFT to be used. Carrying out an FFT results in a transfer function for the object which is a complex-valued set of data. The data is square-window filtered to keep only those frequency components which are present in the source spectrum. This reduces both noise and the amount of data to process in following steps. The data is now arranged into an m vector $\mathbf{f}$, where m is the total number of frequency components kept times the number of spatial channels captured per cross-correlation. These data sets, $\mathbf{f}_i, i = 1,\ldots,n$, where n is the total number of cross-correlations captured, are arranged into an $m \times n$ matrix $\mathbf{F}$:

$$\mathbf{F} = \left[\mathbf{f}_1, \mathbf{f}_2, \ldots, \mathbf{f}_n\right], \tag{3}$$

The columns of $\mathbf{F}$ now contain the transfer functions of the object. To use statistical correlations, some of the columns contain cross-correlations collected with an object at a certain position, call it position 1, other columns contain cross-correlations collected at position 2, and so on.

To make correlations between the columns $\mathbf{F}(\mathbf{f}_i)$ easier to find, we need to reduce the amount of data to analyze without losing any information. One useful method is principle component analysis. First, we perform a singular value decomposition on $\mathbf{F}$ to find an orthonormal set of basis vectors $\mathbf{U}_i, i = 1,\ldots,n$ for each $\mathbf{f}_i$. These basis vectors are arranged in descending order according to their corresponding singular values. Principal component analysis tells us that only the first few basis vectors $\mathbf{U}_i$ are necessary to represent each $\mathbf{f}_i$ to within a certain tolerance. Therefore, we choose to truncate this expansion to a length of $n_{\max}$ sufficient for the accuracy of this analysis. Now the original vectors $\mathbf{f}_i$ can be expressed in terms of the basis vectors $\mathbf{U}_i$ as

$$\mathbf{f}_i = \sum_{j=1}^{n_{\max}} \alpha_{i,j} \mathbf{U}_j, \tag{4}$$

where $\alpha_{i,j} = \mathbf{f}_i^{\dagger} \mathbf{U}_j^{*}$ are the expansion coefficients.

Calculating the expansion coefficients $\left\{\alpha_{i,j}\right\}_{j=1}^{n_{\max}}$ for each $\mathbf{f}_i$ gives us the reduced set of data desired. Each cross-correlation's transfer function is now represented by only five or six expansion coefficients. Since each position of the object has multiple sets of cross-correlations, the expansion coefficients for identical object positions are averaged together. We define the average of the expansion coefficients for each position k as $\left\{\beta_{k,j}\right\}_{j=1}^{n_{\max}}$. One way to quantitatively find statistical correlations among the recorded cross-correlations is to compare the expansion coefficients $\left\{\alpha_{i,j}\right\}_{j=1}^{n_{\max}}$ for each cross-correlation with the average expansion coefficients $\left\{\beta_{k,j}\right\}_{j=1}^{n_{\max}}$ for each object position:

$$\gamma_{i,k} = \sum_{j=1}^{n_{\max}} \left| \alpha_{i,j} - \beta_{k,j} \right| . \tag{5}$$

The object position *k* at which an individual cross-correlation *i* was taken should provide a minimum for that particular value of $\gamma_{i,k}$. For example, if the 14th cross-correlation $\mathbf{f}_{14}$ is from object position 3, then $\gamma_{14,3}$ should be a minimum since the expansion coefficients should be similar to the average expansion coefficients for that object position. For $\left\{\gamma_{14,k}\right\}_{k \neq 3}$, we can expect larger values. In this way, once we have collected several cross-correlation from different object positions, we can identify which object position subsequent cross-correlation are collected from by looking for a minimum $\gamma_{i,k}$.

III.3. EXPERIMENTAL SETUP AND PROCEDURE

We have experimentally verified the validity of the analysis presented above and in Ref. [1] by building the interferometric imaging system outlined in Fig. 1. As explained in Section 2, an interferometer is used for performing cross-correlations between a reference and object signal. In turn, this cross-correlation is used to find the transfer function for the object. Here, we discuss the experimental setup of our Michelson interferometer which we use to find the transfer function produce by an object illuminated by a spatially coherent polychromatic or broadband source.

A point fluorescent source similar to that developed by Liu et al.[15] is used to obtain a broad spectral bandwidth with acceptable spatial coherence. The source is a dye-jet illuminated by the multi-spectral, 2.5 W output of an Argon-ion laser. A sapphire nozzle in the dye-jet provides a laminar dye stream 400 μm thick. The dye used is Rhodamine 590 Chloride (Exciton), also known as Rhodamine 6G. The dye is dissolved in ethylene glycol. The laser is focused in the center of the dye-stream by a 25 × microscope objective to a spot size of 1.6 μm. The idea is to focus the laser beam to the smallest spot possible to simulate the infinite spatial coherence from an ideal point source. Light from the fluorescing dye is re-collimated by the same microscope objective and then filtered by a band-pass absorption filter (Oriel 51302) to filter out the original laser source. The output is a spatially coherent, broad-band beam having a spectrum with a center wavelength of 566 nm and a FWHM of approximately 30 nm. The difference between this light source and the one modeled in our theoretical analysis (Ref. [1]) is that this source has a continuous spectrum instead of several distinct, sharp frequencies. This results in a lower overall SNR for our experimental system, but provides us with a range of frequencies with which to probe our object.

The Michelson interferometer splits the collimated beam produced by the dye source into an object beam and reference beam. This is done using a 1-inch beamsplitter cube (OFR SCL-25-VIR) which is anti-reflection (AR) coated to pass light in the 550-780 nm range. Beyond the beamsplitter, neutral density filters are placed in each path to equalize the total energy reflected from the reference mirror and the object. The reason for placing a filter in each arm of the interferometer is to neutralize the dispersion an individual filter in just one arm would cause. Reflections from the faces of the filters were separated from the image by tilting these surfaces slightly. Lenses, (Thorlabs C110TM-A) with a 6.24 mm focal length and a 0.40 numerical aperture, focus each beam to a diffraction limited spot with a radius of about 5 μm on the object and reference mirror. These lenses are AR coated to pass wavelengths between 350-600 nm. Again, the reason a lens is used in the reference beam is to compensate for the dispersion which would be caused by a single lens in the object beam. The scattered light from the object and reference mirror is then re-collimated by their respective lenses and sent back through the beamsplitter to be recombined, forming an interference pattern that can be detected on a CCD array. For practical reasons, the collection of the scattered light from the object differs from that modeled in Ref. [1] in that here we are probing the object in a reflective geometry instead of a transmissive one.

The reference mirror position or path delay of the reference beam is controlled by two systems. First, we use an electro-motive translator (MPB) with analog closed loop feedback from an inductive position sensor (Kaman Instrumentation) which gives maximum stability and linearity. This system is in turn controlled using a novel interferometric positioning system designed specifically for this experiment. This system uses a second laser (Spectra Physics frequency stabilized He:Ne laser) which propagates slightly above and parallel to the dye-source beam, thus traversing the identical optical path distance. The spatial fringe pattern produced by this He:Ne laser is captured by the CCD array and Fourier transformed to directly extract the phase of the spatial fringes. By maintaining a careful history of this phase, the absolute position of the reference mirror can be found to within 1 nm over the full range of the electro-motive translator (100 μm.) This positioning information is then fed back to the analog feedback system with a 16-bit digital to analog converter to complete the digital feedback loop. This results in our ability to determine the OPD to an absolute accuracy of less than 2 nm and to control the OPD in steps of 5 nm. We obtain this accuracy over the system's complete OPD range of 200 μm which, incidentally, is twice the range of the actual stage movement and is due to the nature of the Michelson type interferometer used.

A scientific-grade CCD array (Princeton Instruments) is used to capture the data from the cross-correlations as well as to capture the fringe pattern produced by the He:Ne laser for the positioning system. This CCD array features active cooling, 16-bits of dynamic range, a full well capacity of 500,000 electrons, and an integrated electro-mechanical shutter. To eliminate excessive mechanical vibrations, we externally mount the shutter to an isolated structure.

To laterally position the sample in the x and y directions, we use a pair of compound flexure stages with piezoelectric drives (Melles Griot NanoFlex™ 17TFC001/MD) which feature zero friction and stiction over a 20 μm range. These stages also rely on analog closed loop feedback by employing inductive sensors (Kaman Instrumentation) for maximum stability and linearity. The sensors are factory calibrated using interferometric techniques which give us an accuracy better than 50 nm, assuming the temperature is stable over the length of the measurement. Note that only x positioning is needed in the experiments discussed this section.

The subwavelength featured object used is the semi-polished back of a GaAs wafer. When viewed under a scanning electron microscope, as shown in Fig. 3, the surface is observed to contain a random pattern of grooves and pits, a result of the chemical etch used in processing. The sharp edges have high spatial frequencies, which provide adequate form dispersion for our system to detect.

This system is very sensitive to noise and changes in the surrounding environment. Therefore everything possible must be done to isolated the system and reduce sources of noise. The system is mounted on a vibration damped optical table (TMC) supported on air pistons. Enclosures are used to isolate the dye source from the interferometer as well as isolating the CCD array. The enclosure used for the interferometer is acoustically and thermally insulated. The temperature of this enclosure is held constant at 77.26 °F using a wire heater with temperature feedback control. All remaining optical paths are covered to prevent dust and air turbulence caused by the air handlers from becoming sources of noise. All mirrors used in the system with exception of the dye-source have a surface flatness to $\lambda/20$ to insure minimal wavefront distortion. A single computer is used to control the positioning of the reference mirror as well as store data collected from the CCD array during the cross correlations. The computer is networked to allow monitoring from a remote location so as not to disturb the experiment while taking data. A schematic of the overall system is shown in Fig. 1.

Our experimental procedure consists of collecting cross-correlations over a square aperture on the CCD array measuring 11×11 pixels to give a total of 121 spatial channels. The cross-correlation of an object as performed with our interferometric imaging system is accomplished by indexing the OPD in steps over the full extent of the "temporal" fringes. The step size, which is 150 nm, is chosen so that the sampling of the interference fringes is near the Nyquist rate. The extent of "temporal" fringes in our system will always be greater than one over the bandwidth of the source and is found by experiment to range between 300 and 1500 samples. For each value of the reference mirror position or OPD, the intensity at each pixel in the 11×11 aperture is integrated for a specified time and then recorded by the computer. This time duration, which is controlled by a mechanical shutter, ranges between 50 and 100 ms, depending on the incident intensity, and is optimized at the beginning of an experiment to utilize the full well capacity of the CCD array. A sample of the interference fringes collected at one pixel versus the OPD is shown in Fig. 2.

Several cross-correlations are collected for each of several object positions as follows. We begin by laterally moving the object to position 1 and collecting a cross-correlation. The object is then laterally shifted by Δx (where Δx is less than one-half of the center wavelength of the scanning light) to position 2 and another cross-correlation is captured. Cross-correlations are collected for up to five different object positions. The entire process is repeated up to 50 times so that redundant data is taken for each object position. This means that each individual object position can have up to 50 cross-correlations associated with it. To maximize the SNR, it is necessary to collect as much information as is reasonably possible. Two factors which limit the amount of data that can be collected are, the amount of data storage space available, and the time it takes to collect the data. It can take up to 12 minutes to collect a single cross-correlation. Thus the time it takes to collect a full set of data (50 cross-correlations) can be as long as 10 hours. It is crucial to make this time as small as possible to avoid any time dependent correlations from entering into our data.

III.4. EXPERIMENTAL RESULTS

The following experimental results indicate subwavelength detection of an object using conventional optics coupled to an interferometric detection system. The resolution limit is being tested with subwavelength translation of the object and indicates resolution to better than $\lambda/10$. Since the accuracy of the positioning stage that moves the object begins to drop off around 50 nm, we are quite sure this is affecting the lower bound on the system's resolution. The actual resolution of our system may be substantially better than our results indicate.

The results of a particular experiment described in Section 3 are shown in Fig. 4. In this experiment, we collect nine cross-correlations at each of five different object positions separated by 50 nm, for a total of 45 cross-correlations. The position of the object is changed after each cross-correlation was collected to avoid correlations between the object position and various time dependent effects (i.e. temperature). The data is then processed as described in Section 2. First a set of averaged basis vectors (β) are calculated for each object position. Then one additional cross-correlation is collected from each object position and compared to the average basis vectors already computed. When Eq. (3) is applied, the α's are taken from this latest set of five cross-correlations and the β's are taken from the first 45 cross-correlations. We use separate sets of cross-correlations to calculate the α's and the β's. This is to ensure the averages (β's) are not biased by the cross-correlations we want to identify. What we are essentially doing by this process, is building a map of nine different transfer functions of the object at each position. Then, by taking additional cross-correlations at previous object positions and determining their transfer functions, we can identify from which object position these latest cross-correlations were taken. We have found that for 50 nm movements of the object (less than one-tenth the wavelength of the scanning light), that we can identify with 100% accuracy the position of the object. Figure 4 shows the results of this experiment for each of five different object positions. Plots 4(A) through 4(E) represent $\{\gamma_{1,k}\}_{k=1}^{5}$ through $\{\gamma_{5,k}\}_{k=1}^{5}$, respectively. The minimum in each plot corresponds to the average position that is closest to the actual position measured. The values of $n_{\max}$ in these plots is 5. Fourteen evenly-spaced frequency components between 490.0 THz and 555.0 THz are used for the analysis. The spacing between the frequencies components is 5 THz. This corresponds to a wavelength range of 540 nm to 612 nm.

Figure 5 shows the accuracy of our interferometric imaging system for different step sizes. In each case, ten cross-correlations from five object positions are measured. Then, the basis vector coefficients used to represent each of the 50 transfer functions are compared to the average coefficients for each object position as in Eq. (3). The percent accuracy shows the percentage of times the object position, determined by the minimum value of γ, correctly corresponds to the actual object position from which the cross-correlation is taken. The preceding analysis is done using five basis vectors ($n_{\max} = 5$) and 14 adjacent frequency components.

Figure 6 shows how the accuracy is affected when the number of basis vectors $n_{\max}$ is decreased. This experiment, as above, had five object positions, and ten measurements at each position. The step size was 50 nm and the number of adjacent frequency components is 14. As can be seen, the results are correct for four or more basis vectors ($n_{\max} = 4$.)

Figure 7 shows that we can get results with 100% accuracy with as few as 8 spatial channels, or pixels. In this plot, $n_{\max} = 5$, the step size is 50 nm, and the number of adjacent frequency components is 14. Note that these 8 pixels are all in a line, perpendicular to the direction of object movement. However, when the pixels are arranged horizontal to the direction of travel, the accuracy decreases substantially.

Figure 8 shows how the accuracy scales with the number of frequency components used in the analysis. Since the whole of the analysis is dependent on multiple frequencies, we obviously should not expect perfect results when using only one frequency component. From this plot, we can see that below 4 frequency components, the results tend to be less than 100% accurate, which confirms our theoretical work. The frequency components are centered around the maximum of 510.0 THz and are spaced 5.0 THz apart.

III.5. CONCLUSION

We have shown that interferometrically detected polychromatic fields scattered by small objects formed of nondispersive materials contain sufficient degrees of freedom for imaging resolution superior to that of monochromatic systems. In addition, we have shown that this extra information can be detected experimentally and used for superresolved object discrimination. Additional studies extending our theoretical analysis to 2-D structures formed of dispersive scatterers and considering the problem of image reconstruction must be performed to apply these degrees of freedom to superresolved optical imaging.

III. 6.FIGURES

Fig. 1.	Interferometric imaging system.
Fig. 2	Intensity at one spatial location versus the position of the reference mirror.
Fig. 3	Semi-polished GaAs surface viewed under a scanning electron microscope at 1600 × magnification.
Fig. 4	γ versus position for five different positions. The impulse responses used to generate Plots (A) through (E) were taken at positions 1 through 5, respectively. Since the minimum in each plot corresponds to the position the impulse response was taken at, that position was correctly determined. For these plots, $n_{\max} = 5$, the number of frequencies was 14, and the number of pixels was 121.
Fig. 5	Accuracy versus step size. $n_{\max} = 5$, number of frequencies is 14, and number of pixels is 121.
Fig. 6	Accuracy versus number of basis vectors $n_{\max}$. Step size is 50 nm, number of frequencies is 14, number of pixels is 121.
Fig. 7	Accuracy versus number of pixels. $n_{\max} = 5$, step size is 50 nm, number of frequencies is 14.

Fig. 8 Accuracy versus number of frequencies. $n_{\max} = 5$, step size is 50 nm, number of pixels is 121.

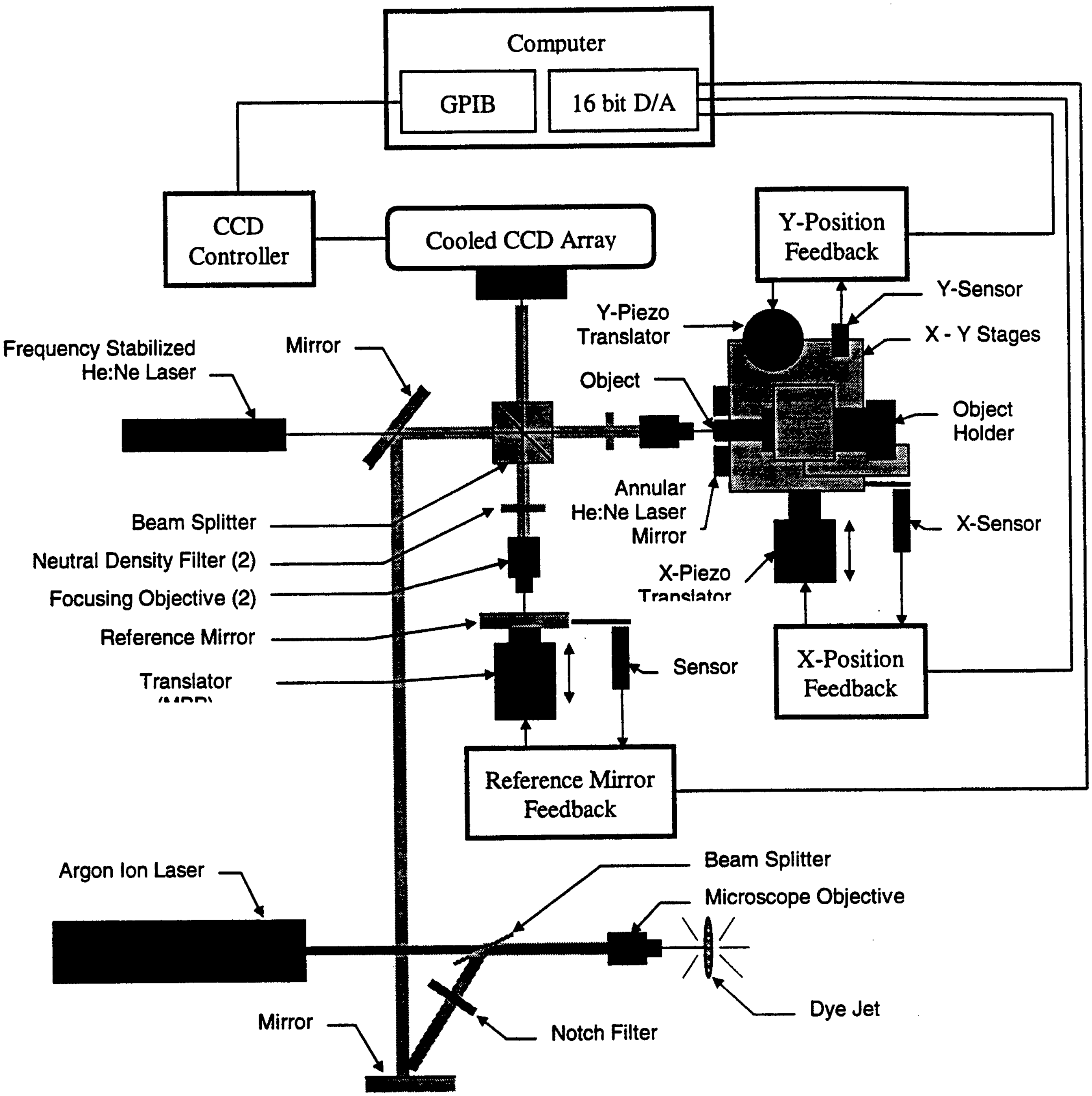

Fig. 1. Interferometric imaging system.

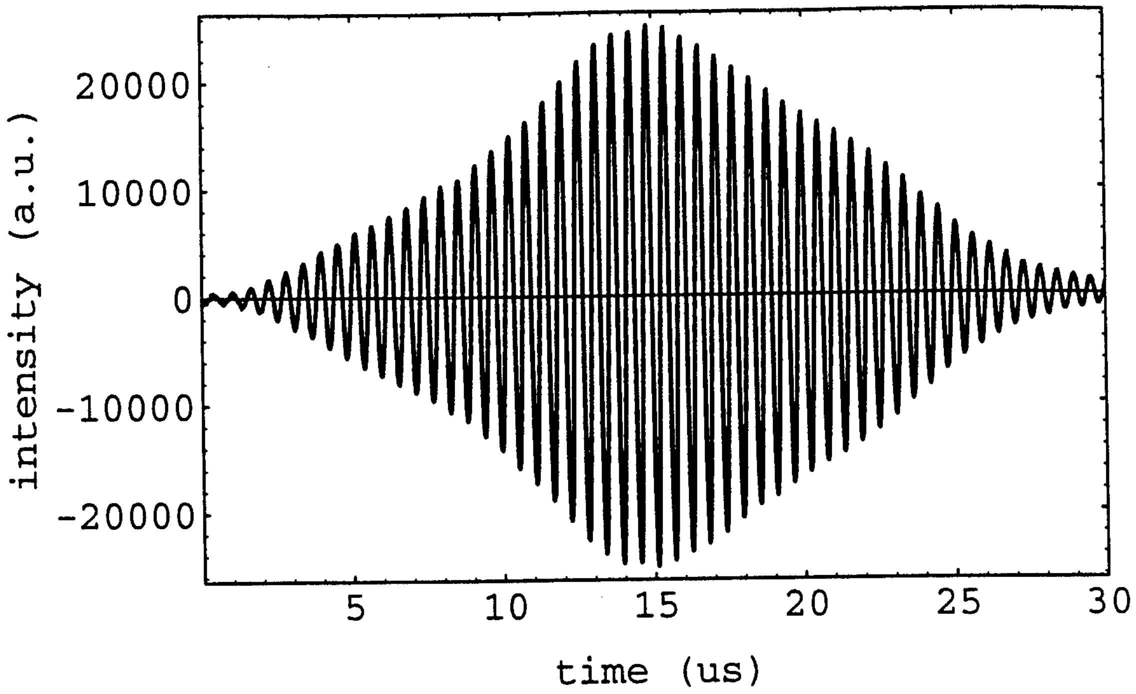

Fig. 2. Intensity at one spatial location versus the position of the reference mirror.

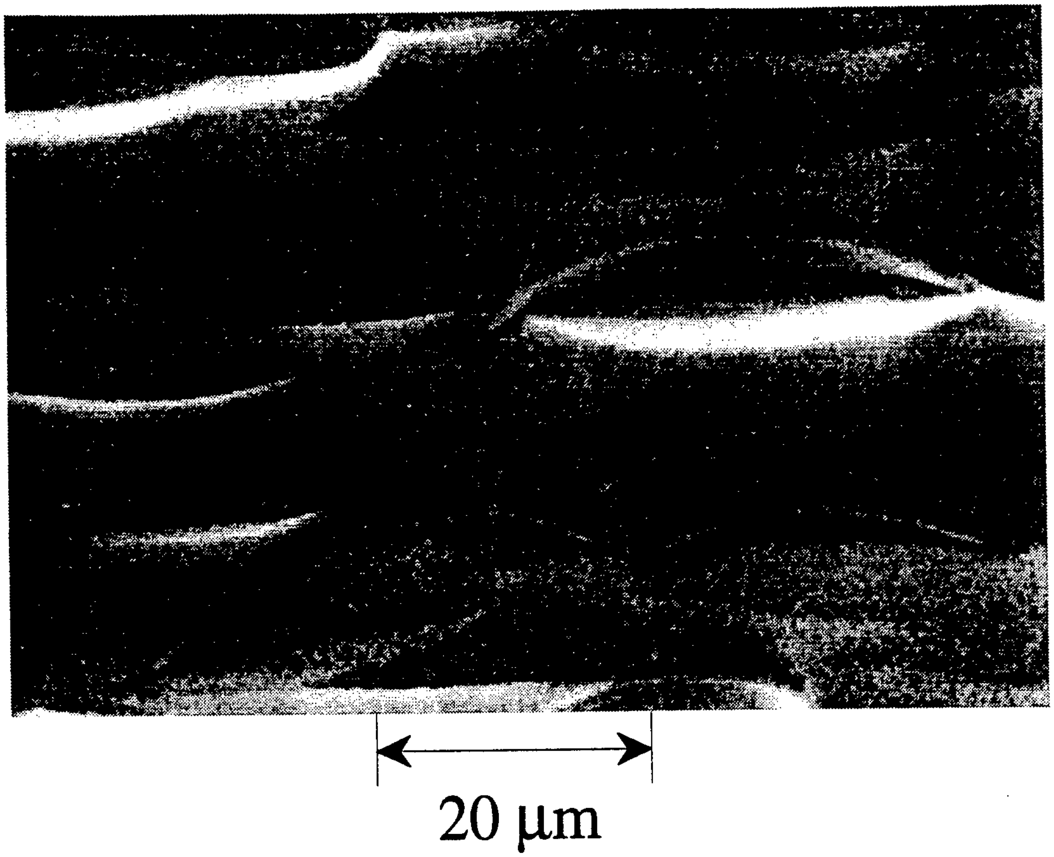

Fig. 3. Semi-polished GaAs surface viewed under a scanning electron microscope at 1600 × magnification.

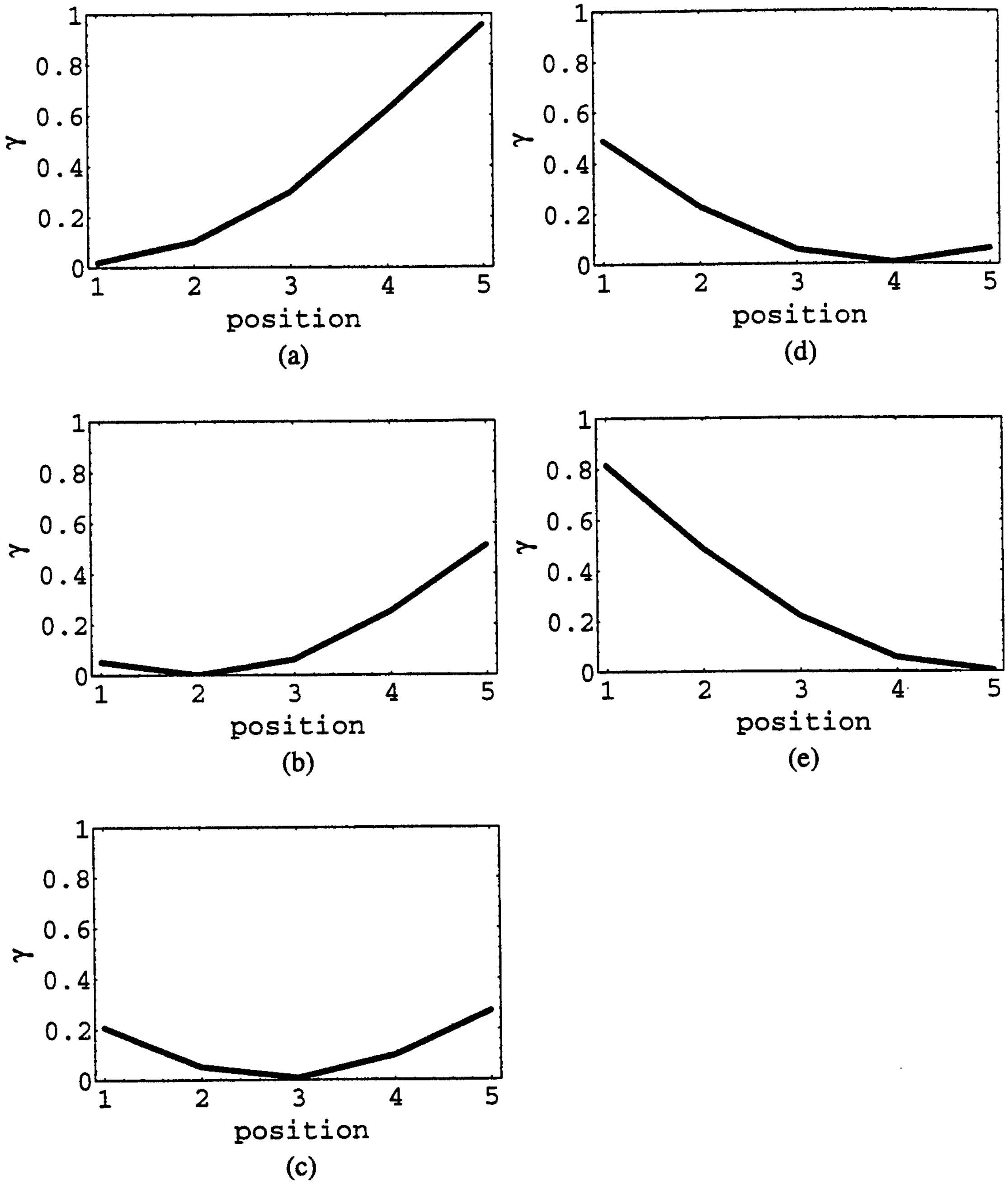

(a) (d) (b) (e) (c)

Fig. 4. γ versus position for five different positions. The impulse responses used to generate Plots (A) through (E) were taken at positions 1 through 5, respectively. Since the minimum in each plot corresponds to the position the impulse response was taken at, that position was correctly determined. For these plots, $n_{max} = 5$, the number of frequencies was 14, and the number of pixels was 121.

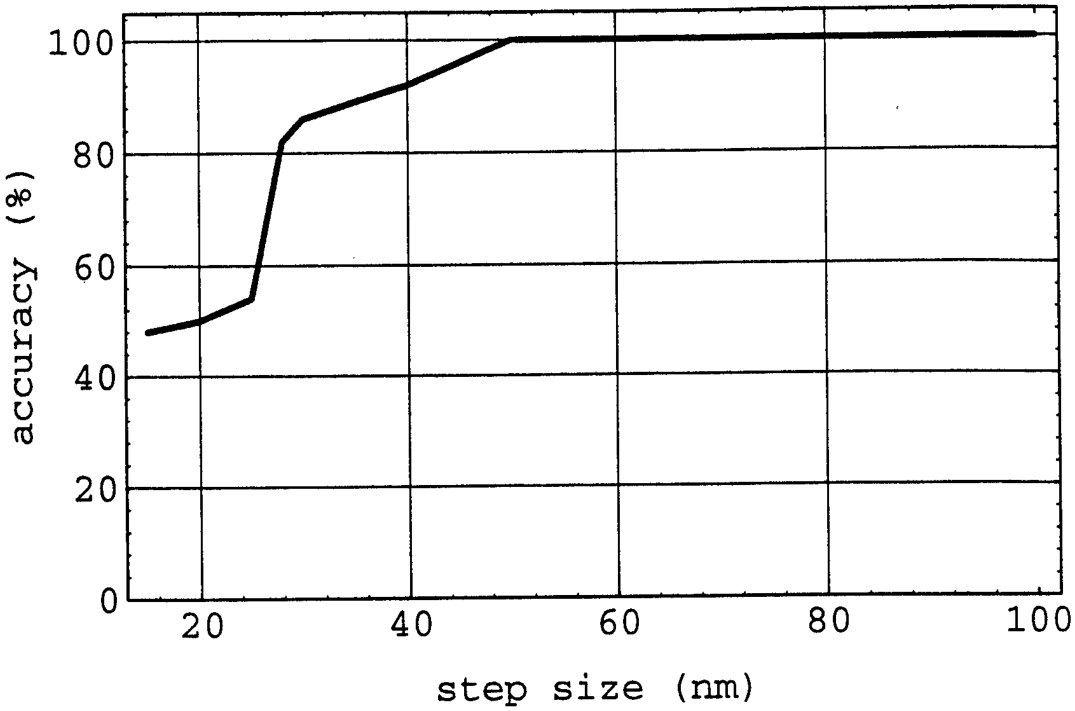

Fig. 5. Accuracy versus step size. $n_{max} = 5$, number of frequencies = 14, number of pixels = 121.

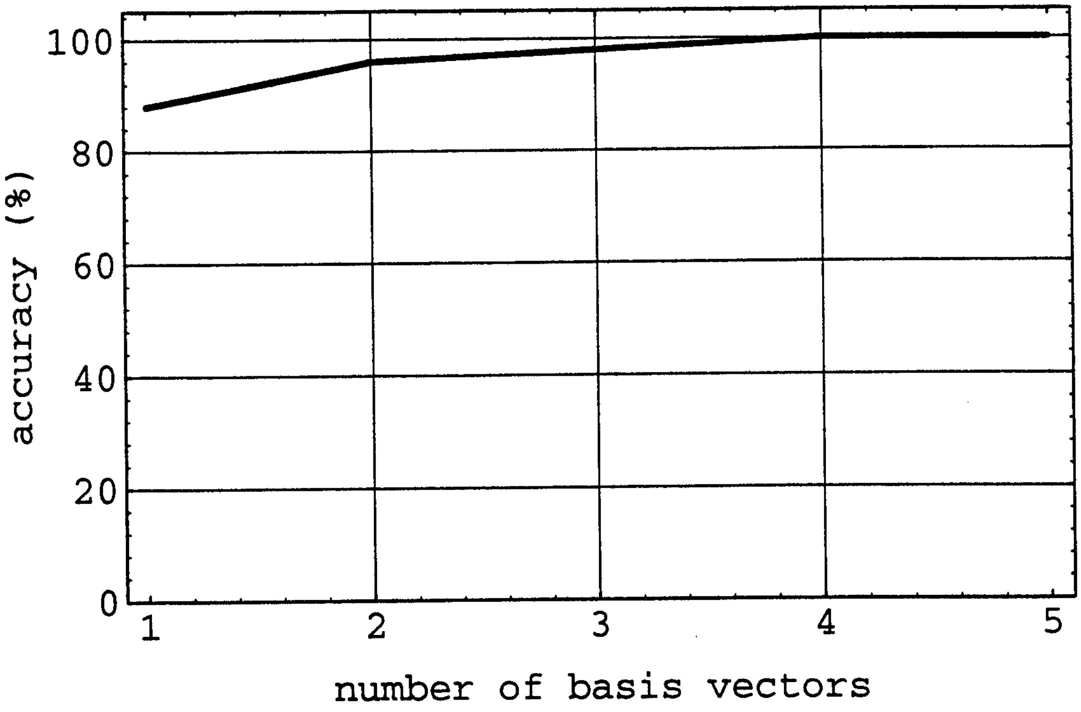

Fig. 6. Accuracy versus number of basis vectors n_{max}. Step size = 50 nm, number of frequencies = 14, number of pixels = 121.

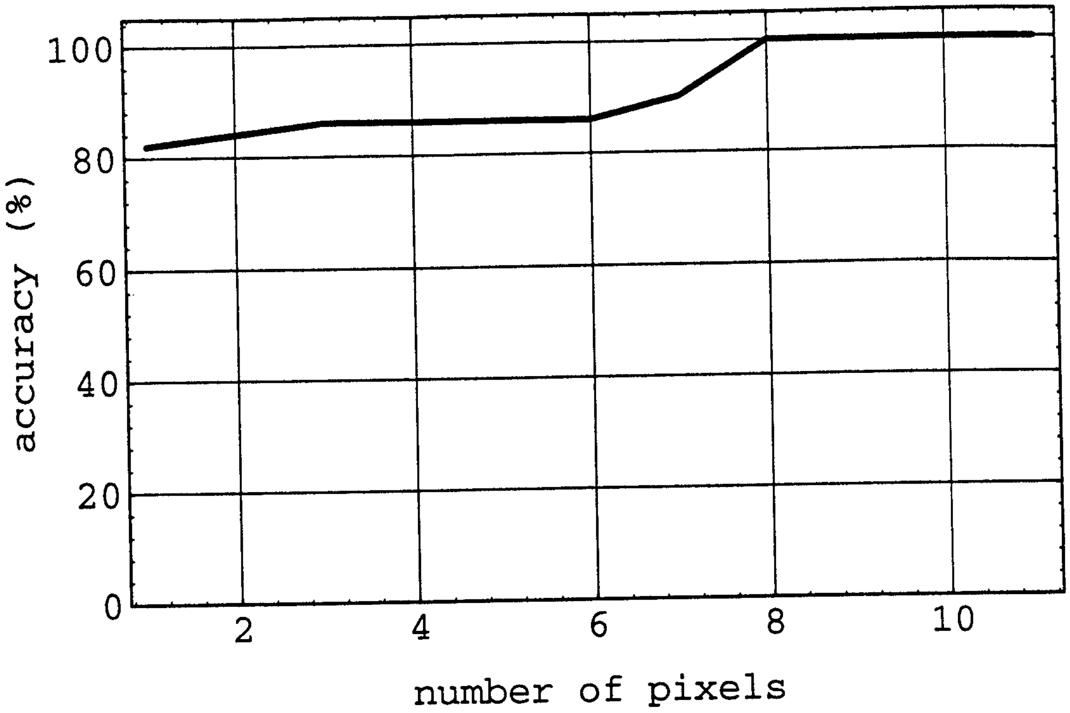

Fig. 7. Accuracy versus number of pixels. $n_{max} = 5$, step size = 50 nm, number of frequencies = 14.

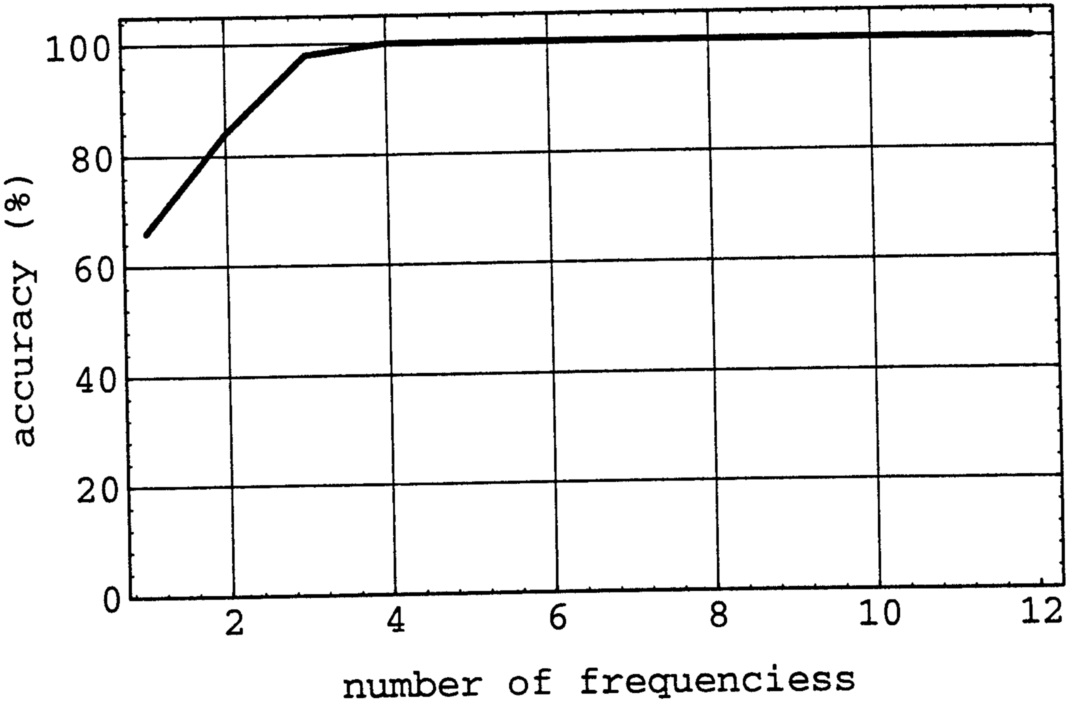

Fig. 8. Accuracy versus number of frequencies. $n_{max} = 5$, step size = 50 nm, number of pixels = 121.

12. D. Huang, E. A. Swanson, C. P. Lin, J. S. Schuman, W. G. Stinson, W. Chang, M. R. Hee, T. Flotte, K. Gregory, C. A. Puliafito, and J. G. Fujimoto, "Optical coherence tomography," Science **254**, 1178 (1991).

13. H. -P. Chiang, W. -S. Chang, and J. Wang, "Imaging through random scattering media by using cw broadband interferometry," Opt. Lett. **18**, 546 (1993)

14. J. A. Izatt, M. R. Hee, G. M. Owen, E. A. Swanson, and J. G. Fujimoto, Optical coherence microscopy in scattering media," Opt. Lett. **19**, 590 (1994).

15. H.-H. Liu, P.-H. Cheng, and J. Wang, "Spatially coherent white-light interferometer based on a point fluorescent source," Opt. Lett. **18**, 678-680 (1993).

16. A. Bearden, M. P. O'Neill, L. C. Osborne, and T. L. Wong, "Imaging and vibrational analysis with laser-feedback interferometry," Opt. Lett. **18**, 238-240 (1993).

17. G. Binning, H. Rohrer, Ch. Gerber, and E. Weibel, "Surface studies by scanning tunneling microscopy," Phys. Rev. Lett. **49**, 57-61 (1982).

18. J. W. Lyding, S. Skala, and J. S. Hubacek, "Variable-temperature scanning tunneling microscope," Rev. Sci. Inst. **59**, 1897-1902 (1988).

19. G. Binning, C. F. Quater, and Ch. Gerber, "Atomic force microscope," Phys. Rev. Lett. **56**, 930-933 (1986).

20. Y. Martin, C. C. Williams, and H. K. Wickramasinghe, "Atomic force microscope-force mapping and profiling on a sub 100-Å scale," J. Appl. Phys. **61**, 4723-4729 (1987).

21. E. Betzig and J. K. Trautman, "Near-field optics: microscopy, spectroscopy, and surface modification beyond the diffraction limit.," Science **257**, 189-195 (1992).

22. F. Zenhausern, Y. Martin, and H. K. Wickramasinghe, "Scanning interferometric apertureless microscopy: optical imaging at 10 angstrom resolution," Science **269**, 1083-1085 (1995).

23. M. A Neifeld, D. Psaltis, and L. Hesselink, "Optical memory: introduction by the feature editors (special section)," Appl. Opt. **35**, 2345-2487 (1996)

24. W. E. Moerner, editor, *Persistent spectral holeburning: science and applications*, Topics in current physics, Vol. 44 (Springer-Verlag, Berlin, 1988).

25. D. Brady and D. Psaltis, "Information capacity of 3-D holographics data storage," Opt. Quantum Electron. **25**, S597-S610 (1993).